17

Effect of Variations in Magma Supply on the Crustal Structure of Mid-Ocean Ridges: Insights from the Western Galápagos Spreading Center

Juan Pablo Canales[1], Robert A. Dunn[2], Garrett Ito[2], Robert S. Detrick[3], and Valentí Sallarès[4]

ABSTRACT

We report results from a seismic refraction experiment across three sections of the Western Galápagos Spreading Center (WGSC) with contrasting axial morphology. Tomography models show the presence of an axial low-velocity zone at the three study areas. After correcting for thermal effects, we estimate the melt content within these regions. At each of the three sites, the largest melt reservoir is located at or just below the Moho, which is 5.25 km deep at site GALA-1 within an axial-valley morphological domain, 6 km deep at GALA-2 in a morphological transitional domain, and 7.5 km deep at GALA-3 within the axial-high domain. The tomography model does not require melt above the Moho at GALA-1, nor at GALA-2, where we find little evidence for crustal melt between the Moho and a melt lens previously imaged at 2.8 km depth. In contrast, at GALA-3 the low velocity anomaly requires the presence of a few percent melt throughout the crust, with two distinct crustal reservoirs: one at the level of the seismically imaged melt lens reflector (1.6 km deep), and a deeper one at 3–4 km depth. The differences in axial melt content and distribution between the three sites are consequences of variations in magma supply, with lower magma supply resulting in less frequent upward migration of melt from the main Moho reservoir to crustal levels. At higher melt supply, transfer of melt to the crust above the main Moho reservoir becomes more frequent, resulting in the formation of distinct crustal melt reservoirs.

17.1. INTRODUCTION

Mid-ocean ridge (MOR) crustal structure is known to depend, among other factors, on spreading rate [*Bown and White*, 1994; *Purdy et al.*, 1992], and comparisons of studies at different MORs have revealed some of the processes underlying this relationship (e.g., see review by *Dunn and Forsyth* [2007]). However, the role of magma supply as a crustal accretion variable independent of spreading rate remains to be quantified. Some MORs, such as the Galápagos Spreading Center (GSC), the Southeast Indian Ridge, or the Reykjanes Ridge, display large variations in axial characteristics in response to gradients in magma supply induced by mantle temperature and/or compositional changes related to hotspots or other mantle anomalies [e.g., *Baran et al.*, 2005; *Canales et al.*, 1997; *Parson et al.*, 1993]. Therefore, hotspot-influenced MORs offer the opportunity to study the effects of magma supply on ridge-crest processes and structure largely isolated from other variables, such as spreading rate [e.g., *Ito et al.*, 2003].

The GSC is a textbook example of a ridge-hotspot system. Between 98° W and 85° W, the GSC displays large geochemical [e.g., *Christie et al.*, 2005; *Cushman et al.*,

[1] *Department of Geology and Geophysics, Woods Hole Oceanographic Institution*

[2] *Department of Geology and Geophysics, University of Hawai'i, Manoa*

[3] *National Ocean and Atmospheric Administration, Office of Oceanic and Atmospheric Research*

[4] *Center for Subsurface Imaging, Institute of Marine Sciences CSIC*

The Galápagos: A Natural Laboratory for the Earth Sciences, Geophysical Monograph 204. First Edition.
Edited by Karen S. Harpp, Eric Mittelstaedt, Noémi d'Ozouville, and David W. Graham.

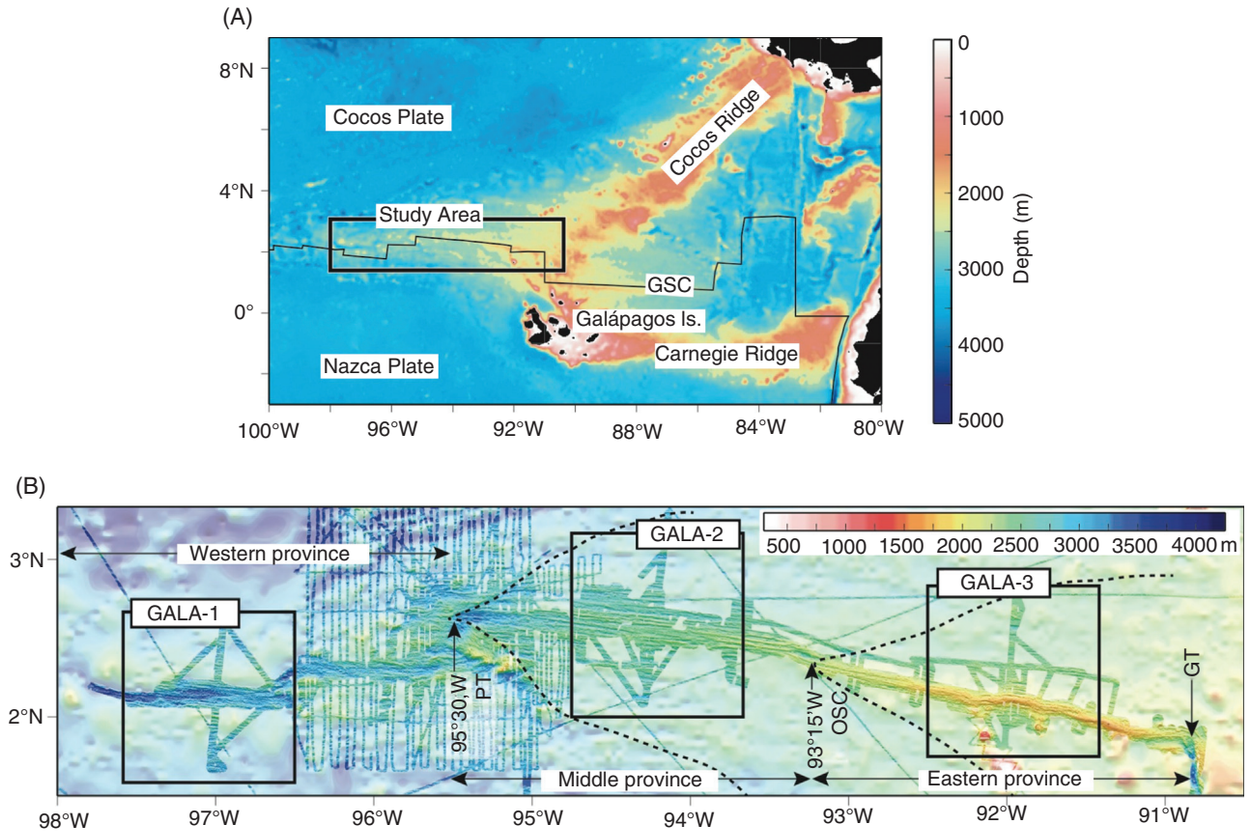

Figure 17.1 (A) Satellite-derived bathymetry map [*Smith and Sandwell*, 1997] of the eastern equatorial Pacific Ocean showing the Galápagos Archipelago and the Galápagos Spreading Center (GSC, solid line), and the study area in the western GSC. (B) Bathymetry map of the western GSC. Data are a compilation of multibeam soundings and satellite-derived bathymetry (light shading) [*Sinton et al.*, 2003]. Boxes correspond to the three areas where seismic refraction experiments were conducted. Dashed lines are propagator pseudofaults. PT: propagator tip. OSC: overlapping spreading center. GT: Galápagos transform.

2004; *Kokfelt et al.*, 2005; *Schilling et al.*, 1982, 2003], morphological [e.g., *Behn et al.*, 2004; *Canales et al.*, 1997; *Sinton et al.*, 2003], and geophysical [*Blacic et al.*, 2004; *Canales et al.*, 2002; *Detrick et al.*, 2002; *Ito and Lin*, 1995] gradients away from the section where the influence of the Galápagos hotspot is strongest (between 92°W and 90°30′W, approximately; Figure 17.1). These gradients arise from changes in mantle temperature and composition along the GSC due to the Galápagos hotspot and delivery of plume material from the hotspot to the ridge [*Canales et al.*, 2002; *Ingle et al.*, 2010; *Ito and Lin*, 1995].

In this paper, we present results from ocean bottom seismic refraction experiments conducted across three sections of the western GSC with contrasting axial morphology, representing the full spectrum of ridge-hotspot influence. At the three sites we determine the characteristics of the axial low-velocity zone representing the accretionary zone, estimate the volume and distribution of melt within the axial crust and uppermost mantle, and relate those results to variations in magma supply along the GSC produced by the Galápagos hotspot. We finalize by comparing our results from the GSC with results from other MORs to extract global conclusions regarding the effect of magma supply on ridge crustal structure.

17.2. THE WESTERN GALÁPAGOS SPREADING CENTER

17.2.1. Tectonics, segmentation, and morphology of the western GSC

The GSC forms the divergent plate boundary between the Cocos and Nazca plates (Figure 17.1A), where seafloor spreading initiated 25 Myr ago [*Hey et al.*, 1977; *Hey*, 1977; *Hey and Vogt*, 1977]. The Galápagos transform fault (also known as the 90.9°W or 91°W transform), located north of the Galápagos Islands, is a first-order discontinuity developed between 2.6 and 3.6 Ma [*Wilson and Hey*, 1995] that divides the GSC into western (WGSC) [e.g., *Detrick et al.*, 2002] and eastern [e.g., *Christie et al.*, 2005] sections

roughly symmetric with respect to the Galápagos hotspot. Along the WGSC, seafloor spreading occurs at intermediate rates, increasing eastward from 53 mm/yr at 97°W to 58 mm/yr at 91°W (full rates) [*Wilson and Hey*, 1995].

Rift propagation and ridge jumps have played a dominant role in the continuous reorganization of the geometry of the spreading axis, with propagation predominantly away from the hotspot and jumps predominantly to the south [*Wilson and Hey*, 1995]. The 95°30′W propagator [*Hey et al.*, 1980, 1986] and the 93°15′W overlapping spreading center (OSC) [*Rotella et al.*, 2009] are two propagating second-order discontinuities that separate three main morphological provinces: western, middle and eastern, following the nomenclature of *Sinton et al.* [2003] (Figure 17.1B).

Axial morphology within each province broadly represents different extents of influence of the Galápagos hotspot [*Canales et al.*, 1997; *Sinton et al.*, 2003]: in the western province, the morphological ridge axis is defined by an axial valley similar to those found at the slow-spread Mid-Atlantic Ridge (MAR), along which the WGSC can reach 1.5 km-deep and 10 km-wide. The middle province is characterized by a transitional morphology without a clear axial high or valley, and with rough seafloor with prominent abyssal hill fabric. At the eastern province, where the influence of the hotspot is most pronounced and the spreading rate is only approximately 10% higher than at the western province, axial morphology is similar to that of the fast-spread East Pacific Rise (EPR), with a broad (approximately 20–30 km), 400–700 m tall axial high. The structure of the ridge in the eastern province is complicated by volcanic lineaments extending between the Galápagos Islands and the WGSC [*Harpp and Geist*, 2002; *Mittelstaedt and Ito*, 2005; *Morgan*, 1978]: where these lineaments intersect the ridge, the axis is displaced southward through a series of small OSCs [*Sinton et al.*, 2003]. The axis is deepest (approximately 3,400 m) in the western province and shoals to approximately 1,600 m in the eastern province as a consequence of both morphological changes and the effect of the Galápagos hotspot swell.

17.2.2. Geochemical and petrological gradients

Long-wavelength variations in isotopic compositions of lavas sampled along the WGSC indicate melting of different mantle sources, with strongest influence of plume material near 92°W [e.g., *Ingle et al.*, 2010; *Schilling et al.*, 2003]. Most of the isotopic variability along the WSGC can be explained with only two mantle source components: a depleted component dominant in the western province, and an enriched component dominating composition of the WGSC in the middle and eastern provinces [*Ingle et al.*, 2010]. The 95°30′W propagator tip thus marks a sharp boundary in mantle source beneath the WGSC [*Ingle et al.*, 2010; *Schilling et al.*, 1982]. The long-wavelength geochemical trends are also locally interrupted at the 93°15′W OSC, where increased variability in lava composition suggests low melt supply and less efficient mixing of melts beneath this axial discontinuity [*Rotella et al.*, 2009].

Major and minor element compositions also show a strong correlation with morphological segmentation of the WGSC: on the basis of K/Ti ratios, *Cushman et al.* [2004] classify WGSC basalts as enriched (E-) MORB, which are dominant east of 92°36′W, transitional (T-) MORB mainly found between 92°36′W and the 95°30′W propagator tip, and normal (N-) MORB dominant in the western province. Models of melting and compositions within each of these MORB groups indicate that N-MORBs are produced by passive mantle upwelling [*Cushman et al.*, 2004; *Ingle et al.*, 2010; *Schilling et al.*, 1982], whereas T- and E-MORBs require increased active, plume-driven flow through a hydrous zone with lower mean extents of partial melting [*Cushman et al.*, 2004; *Ingle et al.*, 2010; *Schilling et al.*, 1982], accompanied by a moderate eastward increase in mantle temperature of approximately 20 °C [*Cushman et al.*, 2004]. Ra-Th-U isotopic disequilibria are consistent with plume influence on GSC lavas resulting from solid mantle flow from the plume to the ridge and subsequent melting of plume material beneath the GSC [*Kokfelt et al.*, 2005], while numerical modeling suggests that the interaction occurs through melt migration from the plume to the ridge along sub-lithospheric channels [*Braun and Sohn*, 2003].

17.2.3. Geophysical gradients

The influence of the Galápagos hotspot along the WGSC is also apparent in a number of geophysical measurements [e.g., *Detrick et al.*, 2002]. Mantle Bouguer gravity anomalies decrease approximately 90 mGal from the western to the eastern province, indicating that the Galápagos bathymetric swell is supported by a combination of an eastward increase in crustal thickness, a decrease in mantle density, and an increase in mantle temperature [*Ito and Lin*, 1995]. Seismic refraction and reflection measurements show that the crustal thickness variation between 97°W and 91°30′W is 2.3 km, which constrains the mantle temperature variation along the WGSC to be approximately 30 °C [*Canales et al.*, 2002].

Multichannel seismic (MCS) reflection imaging along and across the middle and eastern provinces of the WGSC show reflections from an axial melt lens (AML) between 94°20′W and 91°24′W [*Blacic et al.*, 2004]. The AML is 2.5–4.5 km deep west of 92°42′W, and shallower (1.0–2.5 km below seafloor, bsf) east of 92°30′N. Flexural and thermal modeling of axial bathymetry within the eastern province, where the AML is shallow, indicates that the crust below the AML contains 8–20% of melt, and that at least 3% of melt is present in the mantle within a less-than-10-km-wide column extending to depths of 45–65 km [*Blacic et al.*, 2008].

Changes in depth to the magma chamber are accompanied by changes in the characteristics of seismic layer 2A: where the AML is shallower, layer 2A is thin (0.24–0.42 km) and thickens rapidly away from the axis by as much as 150%. In the region where the AML is deeper, layer 2A is thicker (0.36–0.66 km) and thickens off-axis by less than 40%, with no off-axis thickening west of 94° W [*Blacic et al.*, 2004].

17.2.4. Volcanological gradients

Seafloor volcanic morphology and eruptive style along the WGSC also respond to variations in magma supply and crustal structure. Seamount abundance in the axial zone decreases steadily from the western to the eastern province as the hotspot is approached [*Behn et al.*, 2004], although seamount average volume remains relatively constant along the WGSC [*White et al.*, 2008]. Systematic changes in lava flow morphology are also present, from dominantly pillow flows in the western province to a combination of pillows and sheet and lobate flows in the eastern province [*Behn et al.*, 2004]. These variations suggest a transition from point-source to fissure-fed eruptions due to an increase in effusion rates approaching the hotspot [*Behn et al.*, 2004] or, alternatively, due to lengthening of fissure eruptions in response to increased magma supply [*White et al.*, 2008].

17.2.5. Hydrothermal activity

A systematic hydrographic survey conducted along the WGSC indicates that this ridge is a location of anomalously scarce high-temperature venting, with plume incidence about half of that expected for a non-hotspot MOR with similar magma supply [*Baker et al.*, 2008]. Water-column plume mapping discovered active, high-temperature hydrothermal activity in only two locations, though strong plume evidence indicated minor venting from at least six other locations [*Baker et al.*, 2008]. An active high-temperature hydrothermal field is located near 94°W within the middle province (Figure 17.2B), and two others are located near 92°W (Figure 17.2C) [*Haymon et al.*, 2008]. Hydrothermal plume distribution and incidence are apparently uncorrelated with AML depth, suggesting that variations in AML depth along the WGSC are not controlled by differences in the efficiency of hydrothermal cooling [*Baker et al.*, 2008].

17.2.6. Study areas

Our investigation of axial crustal structure is conducted at three locations of the WGSC, one within each of the morphological provinces described in "Tectonics, segmentation, and morphology of the western GSC" (above; Figure 17.1).

GALA-1: This area is centered at 97°W in the western province. Here the axial valley floor reaches depths of 3,400 m, flanked by rift mountains as shallow as 2,550 m and 2,260 m to the north and south, respectively (Figure 17.2A). Seismic crustal thickness along the valley floor is 5.6 ± 0.2 km [*Canales et al.*, 2002]. The presence of an AML reflector here is unconstrained since no MCS surveys have been conducted in this area [*Blacic et al.*, 2004; *Detrick et al.*, 2002].

GALA-2: This area is centered at 94°15′W in the middle province. The spreading axis is 2,470 m deep, flanked by fault-bounded abyssal hills of 200–300 m relief with an average spacing of approximately 5 km (Figure 17.2B). Average seismic crustal thickness 15 km to the north of the axis is 5.9 ± 0.3 km [*Canales et al.*, 2002]. AML depth at 94°15′W is approximately 4 km bsf, but just 10 km to the east and west of this location the AML is 1 km shallower (approximately 3 km bsf) [*Blacic et al.*, 2004].

GALA-3: Centered at 92°W in the eastern province, the spreading axis sits at 1,700 m on a 700-m-high, 30-km-wide axial high, flanked by smooth terrain (Figure 17.2C). Average seismic crustal thickness 25 km north of the axis is 7.45 ± 0.25 km [*Canales et al.*, 2002]. AML depth is 1.75 km bsf [*Blacic et al.*, 2004].

17.3. SEISMIC DATA ACQUISITION

As part of the G-PRIME multidisciplinary experiment [*Detrick et al.*, 2002], in 2000 we conducted three controlled-source, wide-angle seismic refraction experiments at GALA-1, -2, and −3 (Figure 17.2). Each experiment consisted of ocean bottom hydrophone (OBH) deployments and air-gun shooting along one main NS-trending profile across the ridge and one main EW-trending profile parallel to the ridge (along the axis at GALA-1, 15 km to the north at GALA-2, and 25 km to the north at GALA-3). In addition, secondary profiles were shot along transits between the main profiles and along short, on-axis profiles at areas GALA-2 and −3 (Figure 17.2). The seismic source was the *R/V Ewing's* 20-unit air-gun array towed at approximately 8 m depth at a nominal speed of 4.5 knots, with a total volume of 8,755 in^3 (143.5 L), triggered every 210 seconds. Seismic signals were recorded in the OBHs at a rate of 200 Hz. The record sections clearly reveal *P*-wave crustal refractions (*Pg*), Moho reflections (*PmP*), and sub-crustal refractions (*Pn*) (Figure 17.3). Travel times of these three phases were hand-picked, ensuring consistency of phase identification at the crossings of the shooting lines.

17.4. MODELING STRATEGY

The main objective of the experimental layout was two-fold: (1) To estimate the average one-dimensional (1D) velocity-depth function and average crustal thickness

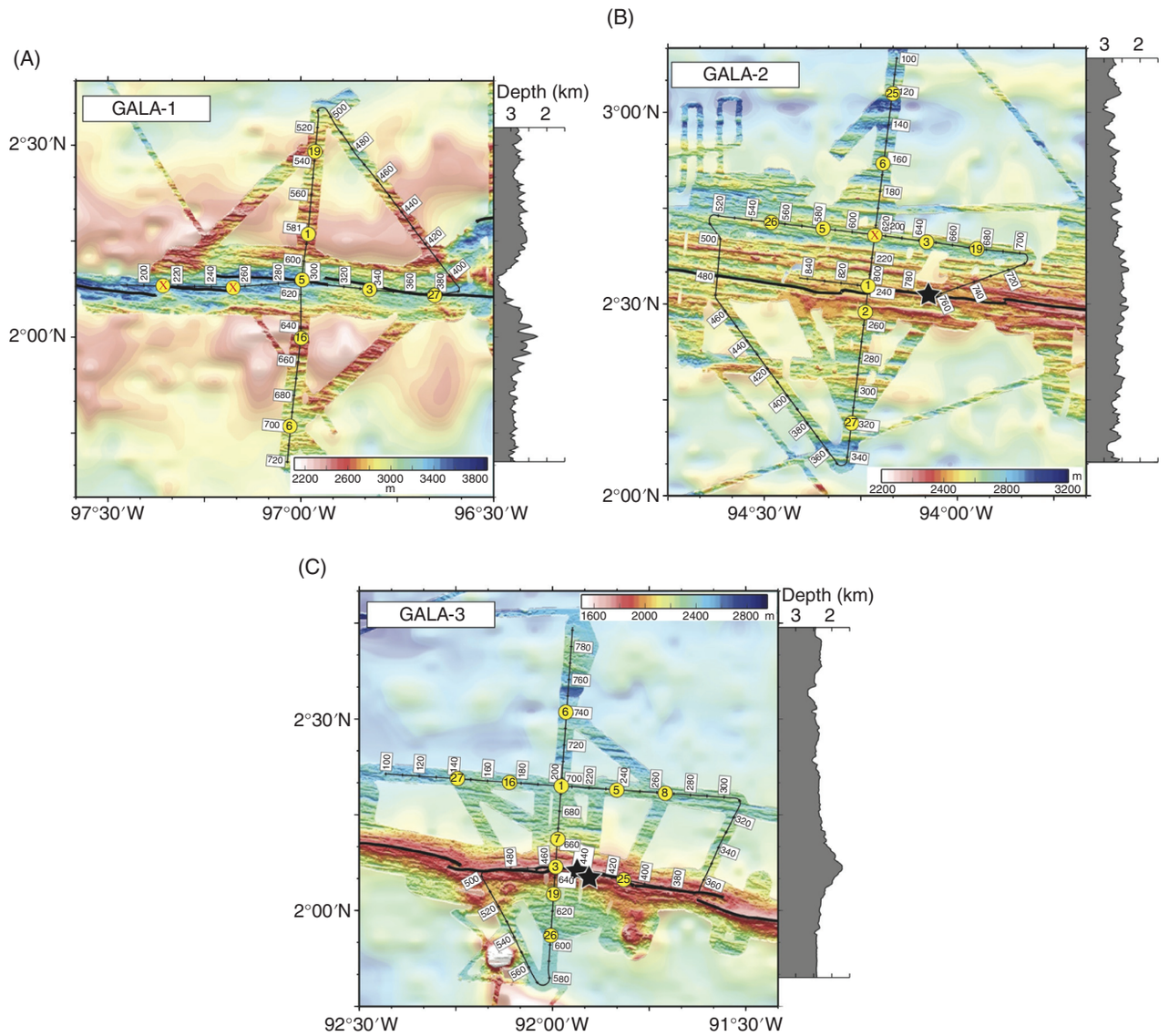

Figure 17.2 Layout of seismic refraction experiments over bathymetry maps (data as in Figure 17.1B) for the three study areas: (A) GALA-1 across an axial valley; (B) GALA-2 across transitional axial morphology; and (C) GALA-3 across an axial high. Solid lines are air-gun shooting lines, with shot numbers indicated every twenty shots. Numbered yellow circles indicate location of OBHs. Yellow circles with red crosses indicate instruments that were either lost at sea or that did not return useful data. Bold solid lines locate the GSC spreading axis. Black stars show location of active hydrothermal fields [*Haymon et al.*, 2008]. Panels on the right show across-axis depth (horizontal axis) versus latitude (vertical axis) along the central NS-trending air-gun profiles.

along the primary off-axis ridge-parallel profiles at each study area; these results have been reported in *Canales et al.* [2002]; and (2) to obtain the two-dimensional (2D) across-axis crustal velocity structure along the primary NS-trending ridge-perpendicular profiles at each study area. Unfortunately, at experiment GALA-2, an internal clock error of the instrument located 15 km to the north of the ridge axis at the intersection between the two main profiles (Figure 17.2B), and noisy data returned by OBH 2 for the range of shots 170–240 along the NS-trending profile (Figure 17.2B) prevented us from obtaining a 2D velocity model along the main NS-trending GALA-2 profile with sufficient ray coverage and resolution at the axial zone. However, recordings from off-line shots in all of the instruments are of good quality (Figure 17.3) and provide sufficient ray coverage (Figure 17.4) for determining the axial structure by using three-dimensional modeling of the complete dataset. Thus, we decided to perform 3D modeling at the three areas for consistency, although the experimental layouts were not specifically designed and

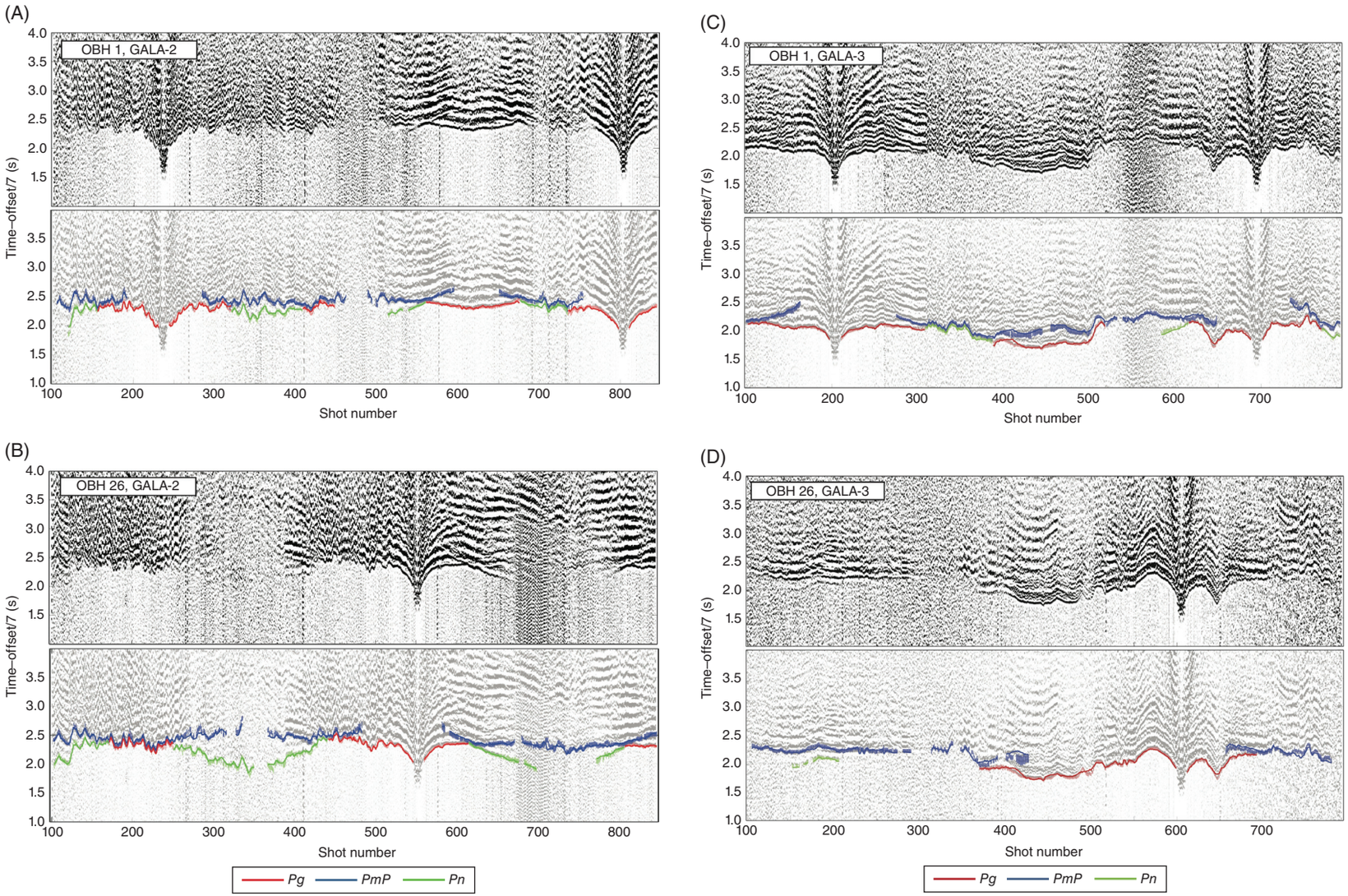

Figure 17.3 Examples of record sections from experiments at GALA-2: (A) OBH 1, (B) OBH 26; and GALA-3: (C) OBH 1; and (D) OBH 26. Top panels show band-pass filtered (5–20 Hz) record sections with reduction velocity of 7 km/s. Bottom panels show picked (vertical ticks with height twice the assigned uncertainty) and predicted traveltimes (solid lines) over record sections. Red are *Pg* picks, blue are *PmP*, and green are *Pn*.

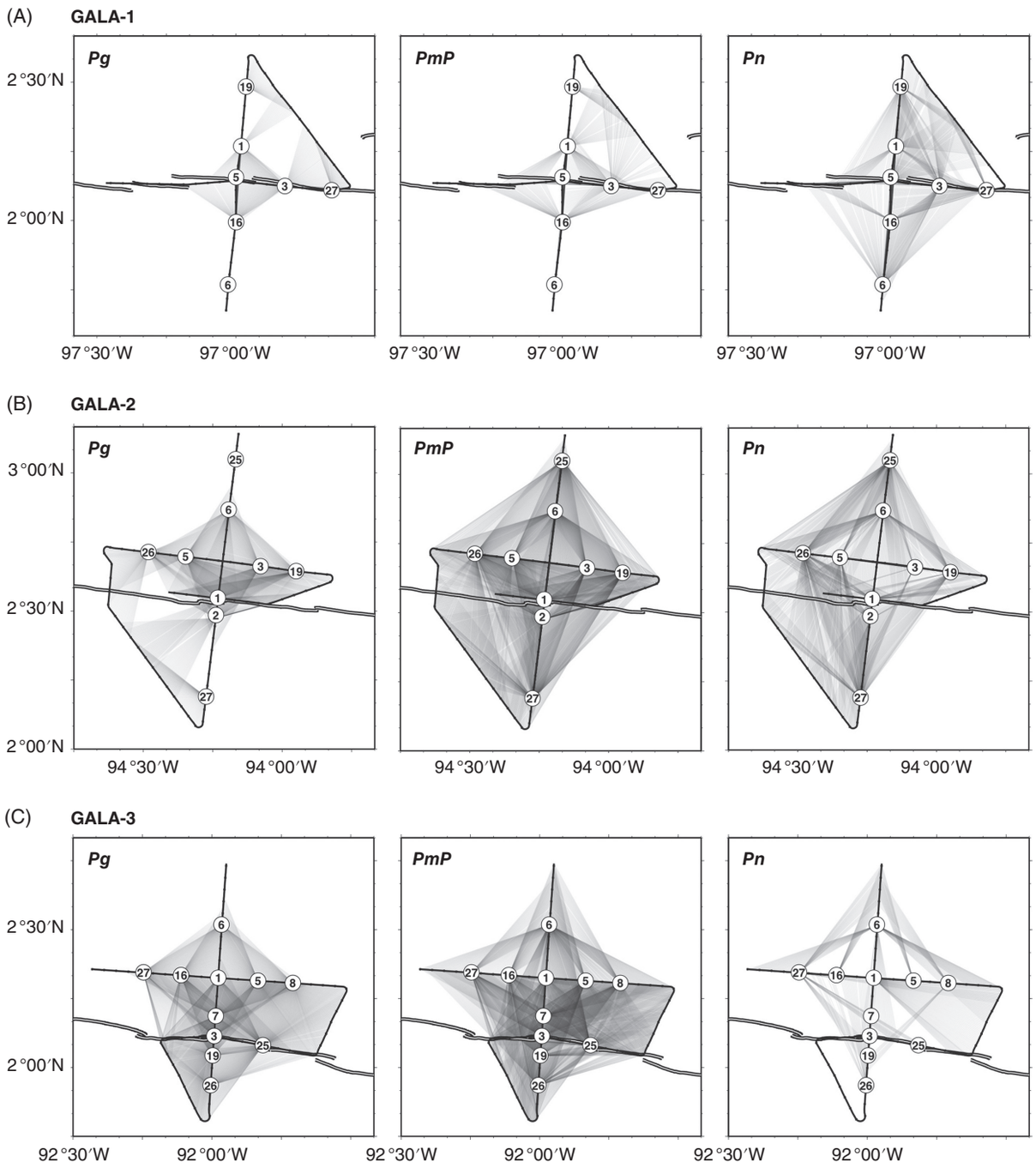

Figure 17.4 Plan view of ray paths (gray lines) connecting each shot-receiver pair used in the inversions for the three study areas: (A) GALA-1; (B) GALA-2; and (C) GALA-3. Numbered circles are OBHs. Solid lines are shot profiles. Thick black-and-white lines locate the GSC spreading axis.

Table 17.1 Modeling parameters[a]

	GALA-1	GALA-2	GALA-3
Forward problem parameterization:			
$[N_x, N_y, N_z]$	[331, 331, 41]	[301, 391, 41]	[331, 331, 41]
$[\Delta_x, \Delta_y, \Delta_z]$ (m)	[333, 333, 250]	[333, 333, 250]	[333, 333, 250]
Inverse problem parameterization:			
$[N_X, N_Y, N_Z]$	[111, 111, 21]	[21, 44, 21]	[45, 74, 21]
$[\Delta_x, \Delta_y, \Delta_z]$ (m)	[1,000, 1,000, 500]	[5,000, 3,000, 500]	[2,500, 1,500, 500]
Inversion parameters:			
σ_u	0.5	0.3	0.19
λ_u	25	50	80
$[\tau_x, \tau_y, \tau_z]$ (m)	[1,500, 1,500, 750]	[7,500, 4,500, 750]	[3,750, 2,250, 750]
n_{iter}	5	5	9

[a] $N_{x, y, z}$: number of nodes; $\Delta_{x, y, z}$: grid spacing; σ_u: a priori uncertainty of slowness; λ_u: weighting scalar for spatial smoothing; $\tau_{x, y, z}$: spatial smoothing lengths; n_{iter}: number of iterations. For definitions of the spatial smoothing parameters see *Dunn et al.* [2005].

optimized for 3D imaging, and the highest resolution occurs along 2D profiles oriented across the ridge.

17.4.1. Tomography method

We use the nonlinear iterative tomography method of *Dunn et al.* [2005] to invert refraction (P_g and P_n) and reflection (P_MP) travel-time data. This method can simultaneously solve the 3D slowness structure, the depth of a reflecting interface, and the *P*-wave seismic anisotropy structure. Readers are referred to *Dunn et al.* [2005] for details on the formulation of the forward and inverse problems. The parameters used in the discretization of both the forward and inverse problems, as well as relevant parameters for the inverse problem, are listed in Table 17.1.

17.4.2. Starting velocity models

At each study area, we conducted 1D inversions to obtain the best average structure at each site. We used the off-axis 1D results of *Canales et al.* [2002] as starting models for the 1D inversions. The resulting velocity-depth functions from each study area were then averaged to create a starting model for the 3D inversions common to all three of the study areas, with the only difference being the crustal thickness: 5.25 km at GALA-1, 6.0 km at GALA-2, and 7.5 km at GALA-3 (Figure 17.5).

17.4.3. Anisotropy

For simplicity and to reduce the number of model parameters in the inversion, we did not explicitly solve for anisotropy. Instead, we included anisotropy in the velocity models only in the cases where travel-time residuals showed a dependence on source-receiver azimuth that could be attributed to anisotropic structure. In these cases, the imposed anisotropy structure remains fixed throughout the inversion iterations.

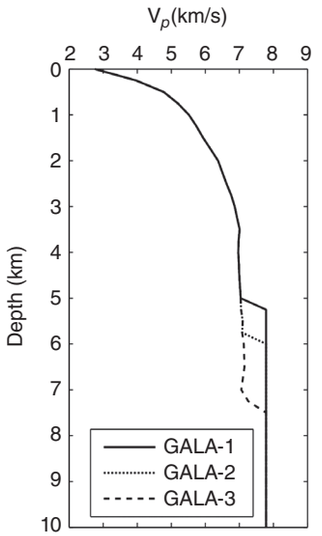

Figure 17.5 One-dimensional structures used as starting models at each site. Crustal thicknesses are 5.25, 6.0, and 7.5 km for GALA-1, GALA-2, and GALA-3, respectively.

Upper crustal anisotropy: Traveltime residuals predicted by the isotropic 1D models (Figure 17.5) for *Pg* rays traveling in the upper 3 km of the crust show a dependence on source–receiver azimuth θ that can be represented by a cos(2θ) function (Figure 17.6A), which is commonly accepted as indicative of azimuthal seismic anisotropy [e.g., *Dunn and Toomey*, 2001]. This dependence is apparent for data from areas GALA-2 and GALA-3, but not GALA-1 (Figure 17.6A). In areas

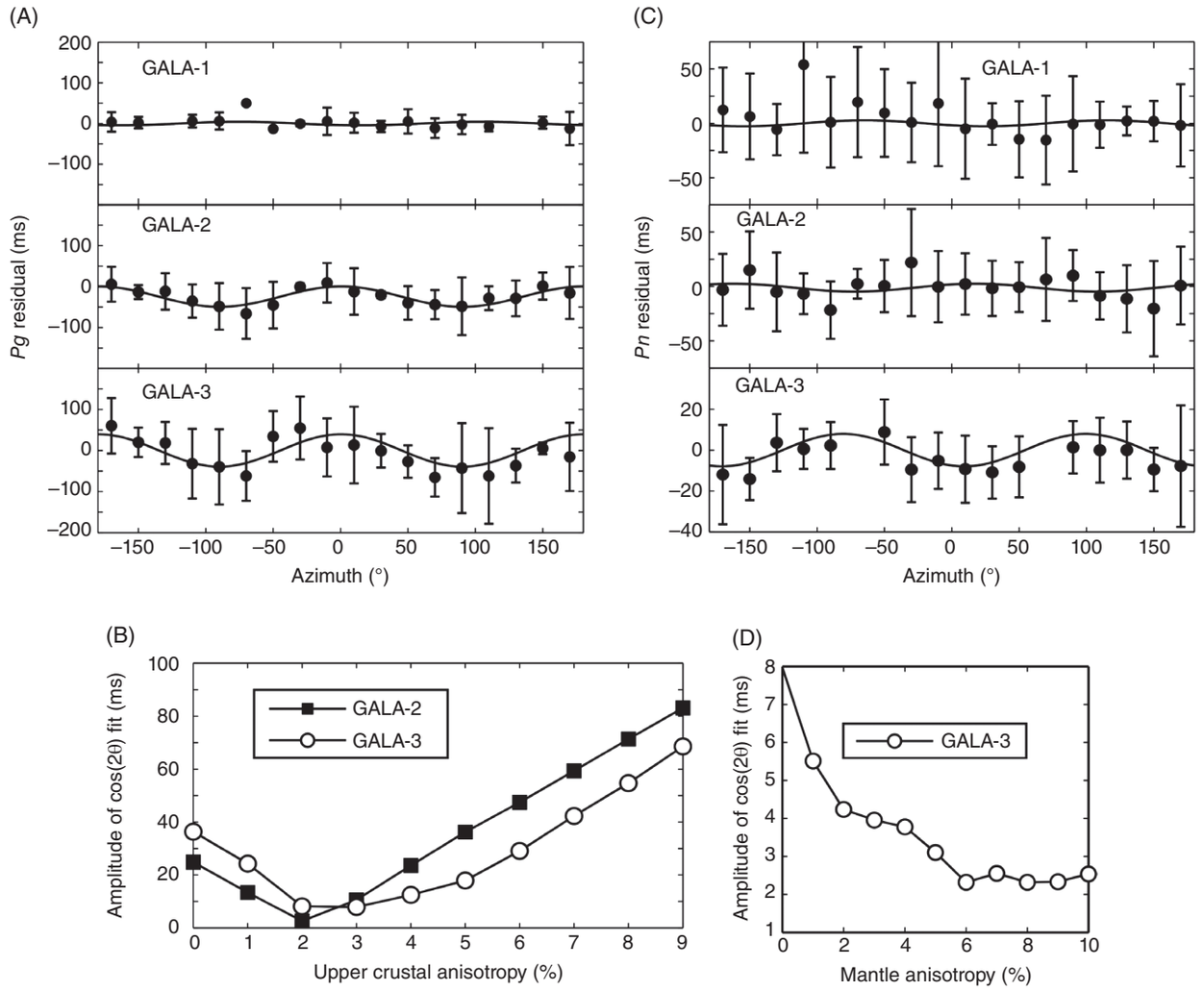

Figure 17.6 (A) Travel time residuals of *Pg* arrivals corresponding to rays turning within 0–3 km depth range as a function or source-receiver azimuth (θ) for the isotropic 1D starting models of Figure 17.5. Residuals were averaged in 20-degree bins, and error bars indicate one standard deviation of the values within each bin. Solid lines are least-squares fits to the data points using the function $A \cdot \cos(2\theta - \Delta)$, where A is amplitude in ms and Δ is deviation in degrees from the spreading direction ($\theta = 0$ degrees). (B) Variation of A for *Pg* residuals as a function of percentage of upper crustal (0–3 km depth range) anisotropy with fast direction parallel to the ridge axis ($\Delta = 90$ degrees) calculated for areas GALA-2 and −3. (C) Same as A but for *Pn* travel time residuals obtained after 3D inversions using the isotropic 1D starting models of Figure 17.5. (D) Variation of A for *Pn* residuals as a function of percentage of mantle anisotropy with fast direction 013–193°N ($\Delta = 9$ degrees) calculated for area GALA-3.

GALA-2 and GALA-3, the residuals are best explained by 2% anisotropy in the upper 3 km of the crust, with the fast direction (90 degrees) aligned parallel to the ridge axis (Figure 17.6B). This upper crustal anisotropy is easily explained by the presence of ridge-parallel cracks and fissures [e.g., *Dunn and Toomey*, 2001; *Sohn et al.*, 1997]. Based on these results, our 3D inversions for areas GALA-2 and GALA-3 include an imposed *ad hoc* anisotropic structure of 2% with fast direction parallel to the ridge axis in the 0–3-km depth range. The apparent lack of upper crustal anisotropy in the GALA-1 area (Figure 17.6A) could be due to the poorer distribution of source-receiver azimuths and ray coverage in the upper crust (Figure 17.4A). Our tests indicate that results for GALA-1 are not significantly different between isotropic or anisotropic cases. Therefore, since the data does not require crustal anisotropy (Figure 17.6A), inversions for GALA-1 presented here are isotropic.

Mantle anisotropy: The presence of anisotropy at mantle levels was evaluated after conducting 3D inversions

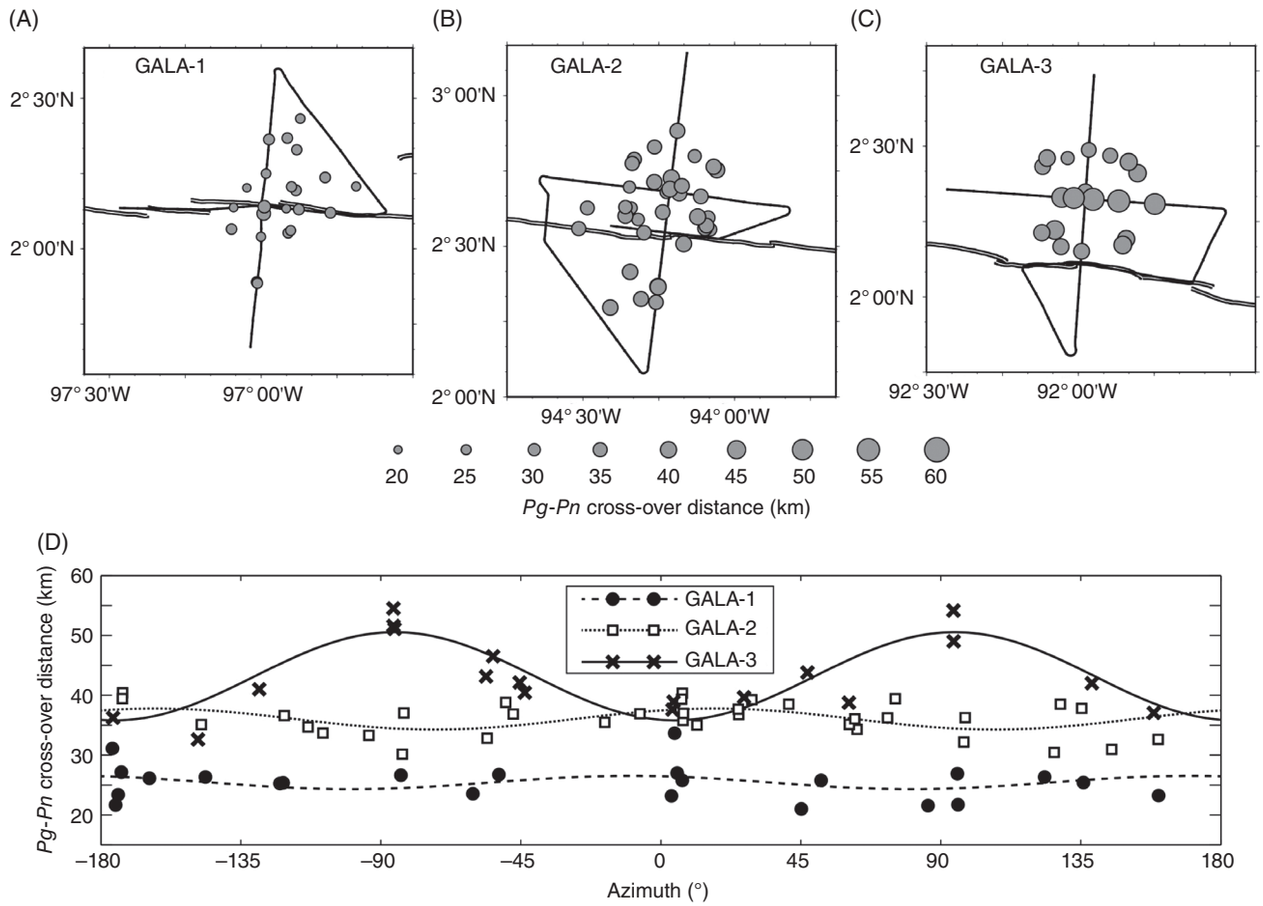

Figure 17.7 Measurements of *Pg-Pn* crossover distance. A, B, and C show map views of the locations of the mid-points of the shot-receiver pairs corresponding to the *Pg-Pn* cross-over (gray circles), with symbol size scaled according to *Pg-Pn* cross-over distance. Solid lines are air-gun profiles, and black-and-white lines locate the GSC spreading axis. (D) Plot of *Pg-Pn* crossover distance versus source-receiver azimuth (degrees clockwise from north). Solid lines are least-squares fits to the data points using a $\cos(2\theta)$ function.

assuming isotropic velocity models and inspecting the travel time residuals for *Pn* arrivals. Only *Pn* residuals from the GALA-3 area show dependence on source-receiver azimuth that can be represented by a $\cos(2\theta)$ function, with fast direction of 009–189 degrees clockwise from the spreading direction (Figure 17.6C). This azimuthal mantle anisotropy is similar to that found in the vicinity of other MORs [e.g., *Toomey et al.*, 2007] and is commonly attributed to the alignment of the *a* axis of olivine crystals in the direction of plate spreading [e.g., *Christensen and Salisbury*, 1979]. Results from inversions for GALA-3 using different amounts of mantle anisotropy show that the $\cos(2\theta)$ pattern of *Pn* residuals becomes negligible given the travel-time uncertainties for ≥6% of mantle anisotropy (Figure 17.6D). Therefore, inversions for GALA-3 presented here include an imposed *ad hoc* anisotropic structure below the Moho of 6% with fast direction at 9 degrees clockwise from the spreading direction, which is similar to that found at other fast-spreading segments [e.g., *Toomey et al.*, 2007].

17.4.4. Crustal thickness

The Moho was approximated as a first-order step from crustal to mantle velocities across a reflecting interface. We did not invert for 3D spatial variations in Moho depth because the data do not show evidence for significant crustal thickness variations within each of the study areas. This was assessed by inspecting the *Pg-Pn* crossover distance, which depends primarily on crustal thickness [e.g., *Shearer*, 1999]. At GALA-1 and GALA-2 the observed crossover distances are relatively homogeneous (26 ± 3 km and 36 ±3 km, respectively) and do not have a discernible spatial pattern (Figure 17.7A, B, D). At GALA-3 we find a wider range of crossover distances (42 ±6 km), with larger values (i.e., presumably thicker crust) occurring approximately 15 km to the north of the ridge axis, and lower values (i.e., presumably thinner crust) occurring closer to the ridge axis and farther to the north (Figure 17.7C).

Table 17.2 Traveltime fit statistics

	GALA-1	GALA-2	GALA-3
***Pg* picks**:			
N	1,036	2,721	4,298
χ^2	1.65	0.93	1.35
RMS (ms)	41	21	19
***PmP* picks**:			
N	860	4,244	4,440
χ^2	1.02	0.87	0.81
RMS (ms)	52	33	22
***Pn* picks**:			
N	1,133	2,033	688
χ^2	1.34	1.26	0.62
RMS (ms)	57	34	14
***All* picks**:			
N	3,029	8,998	9,426
χ^2	1.36	0.98	1.04
RMS (ms)	50	30	20

However, when displayed against shot-receiver azimuth θ, GALA-3 *Pg*-*Pn* crossover distance measurements show a well-defined cos(2θ) pattern, which we interpret as being caused by upper mantle anisotropy. This is because crossover distance is proportional to $\sqrt{\frac{v2+v1}{v2-v1}}$, where $v1$ and $v2$ are the velocities above and below the Moho, respectively. Assuming $v1 = 7.0$ km/s, an average mantle velocity of $v2 = 7.8$ km/s, and 6% mantle anisotropy, the expected ratio between the crossover distance measured along the fast and slow direction of propagation in the mantle is 0.75, comparable to what we observe in the GALA-3 area (36km/51km = 0.71, Figure 17.7D). Therefore, based on these analyses, we did not allow the 3D inversions to produce spatial variations in crustal thickness within each study area, but we allowed the Moho to move up or down as a flat interface after each iteration during the 3D inversions.

17.5. RESULTS

The 3D inversions converge to models that produce a statistically significant reduction in the misfit of the observations, measured as

$$\chi^2 = \frac{1}{N}\sum_{i=1}^{N}\left(\frac{\delta t_i}{\sigma_i}\right)^2$$

where δt_i and σ_i are the travel-time residual and uncertainty, respectively, and N the number of observations. A value of $\chi^2 = 1$ indicates that the calculated travel times fit within the uncertainty bounds; thus, $\chi^2 \approx 1$ was considered an acceptable fit to the data. Traveltime residual statistics are given in Table 17.2, and the histograms of the root mean squared (RMS) residuals for both the starting and preferred models are shown in Figure 17.8. Some examples of the predicted travel-time curves compared to the picks are shown in Figure 17.3.

17.5.1. GALA-1

The velocity structure across the ridge axis in the GALA-1 area shows velocities of 3 km/s increasing to 6 km/s in the upper 2 km of the crust (Figure 17.9A), with localized low-velocity anomalies within this depth range (e.g., at $Y = -15$ and 15 km; Figure 17.9B). At the ridge axis ($Y = 0$ km) at depths of below 2 km, velocities of 5.5–6.5 km/s indicate the presence of a 5-km-wide low-velocity zone (LVZ) at mid- and lower-crustal levels extending down to the Moho (5.25 km depth). Below the Moho, axial mantle velocities are also depressed with respect to off-axis values, defining a mantle LVZ approximately 15 km wide (Figure 17.9B).

In plan view, the axial crustal LVZ extends along the ridge axis to the west of the main NS profile (Figure 17.9C). The sub-Moho LVZ also appears to extend along the ridge axis, although its amplitude is apparently greatly reduced along the ridge away from the main NS profile (Figure 17.9D), probably due to the low density of rays constraining this part of the model (Figure 17.4A).

17.5.2. GALA-2

In the GALA-2 area, upper crustal structure (0–2 km depth) shows across-axis velocity variations that are smaller in magnitude than those of GALA-1 (Figure 17.10A, B). Upper crustal velocities that are faster than the starting model are found away from the axis, while the axial region

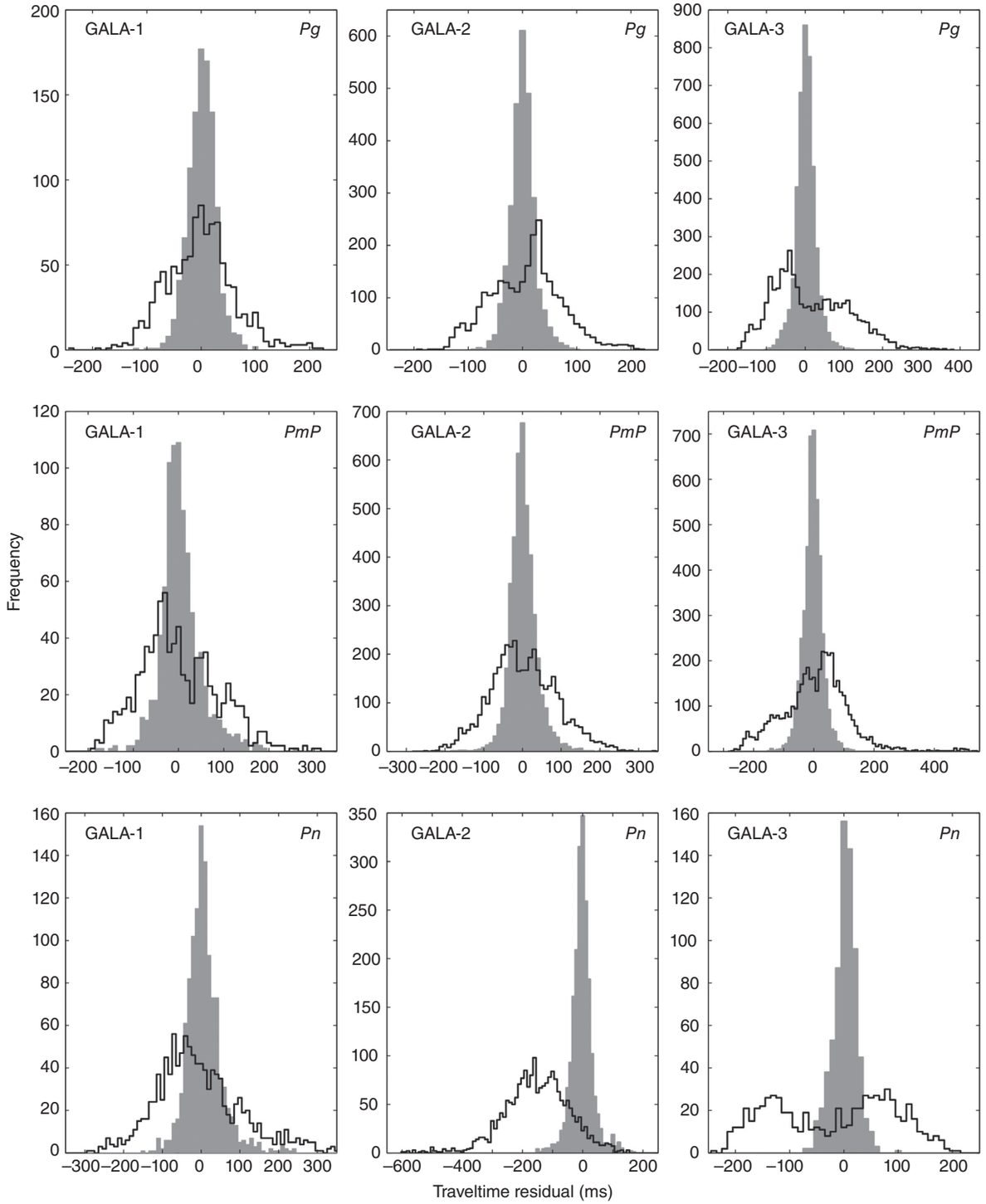

Figure 17.8 Histograms of traveltime residuals by seismic phase for the three study areas. Solid line corresponds to residuals predicted by the 1D models of Figure 17.5. Shaded histograms correspond to residuals predicted by the preferred 3D models shown in Figures 17.9, 10, and 11.

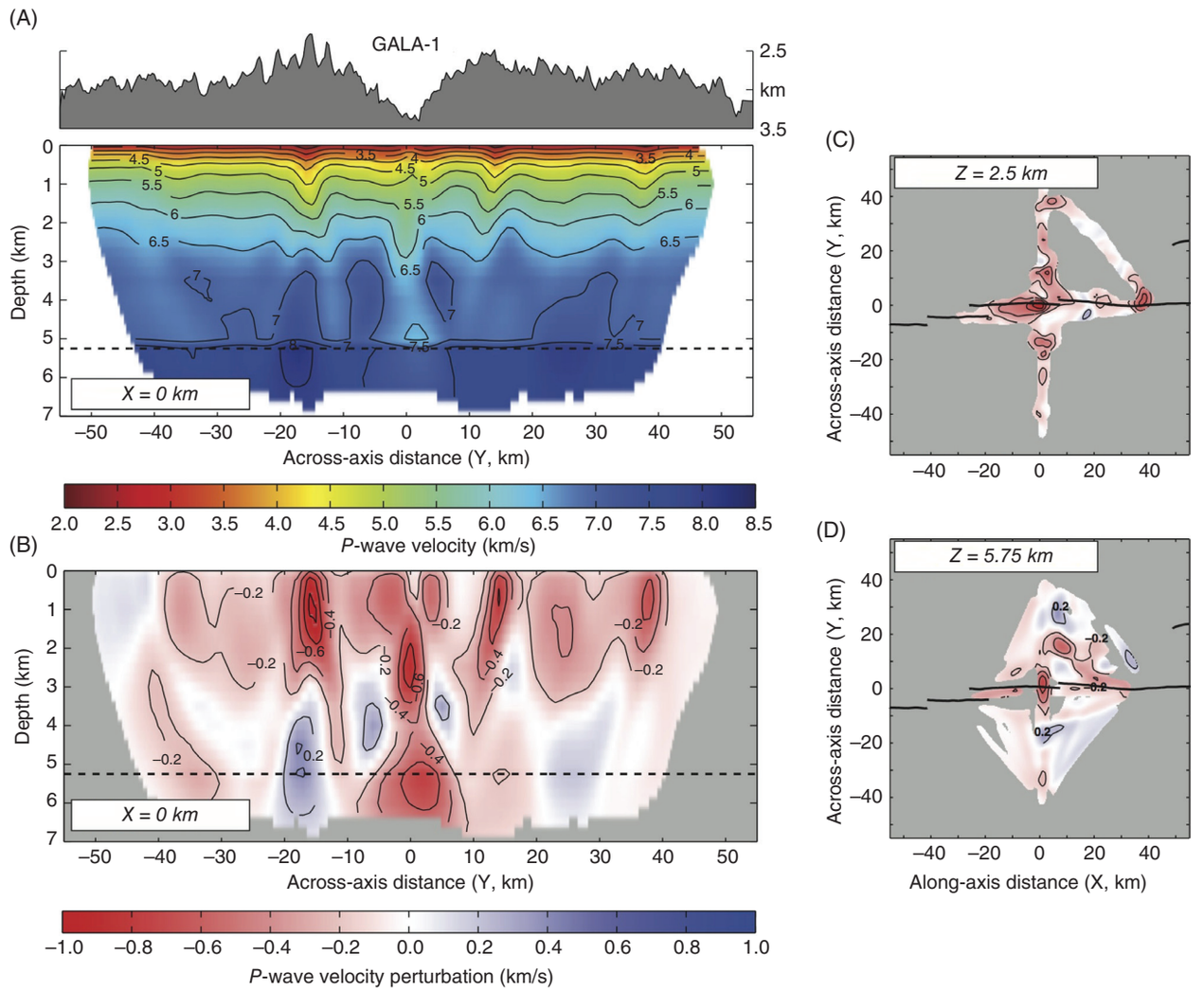

Figure 17.9 Preferred 3D model for GALA-1. (A) *P*-wave velocity model along the main NS profile ($X = 0$ km), with contours every 0.5 km/s. Dashed line corresponds to the Moho reflector. Panel on top shows the bathymetry along the profile. (B) *P*-wave velocity variations with respect to the starting 1D model contoured every 0.2 km/s. C and D show depth slices of the velocity perturbation at 2.5 and 5.75 km depth, respectively. Solid line shows the spreading axis.

shows moderately slower velocities in the upper approximately 1.5 km of the crust.

At mid- and lower-crustal depths, axial velocities increase from 6.2 km/s at 2 km depth to 6.9 km/s just above the Moho. These velocities are approximately 0.4 km/s slower than off-axis velocities at similar depths, thus defining a 10-km-wide axial LVZ. The top of this LVZ roughly coincides with the depth of the imaged AML reflector (Figure 17.10B). This crustal LVZ extends along the ridge axis within our survey area, although decreasing amplitude toward the edges of the model is a consequence of poorer ray coverage in those regions of the model (Figure 17.4B).

At sub-Moho levels, the LVZ is broader (15 km on average) than it is above in the crust (Figure 17.10B). The sub-Moho LVZ is present beneath the ridge axis within the survey area and displays along-axis variations in width and anomaly amplitude.

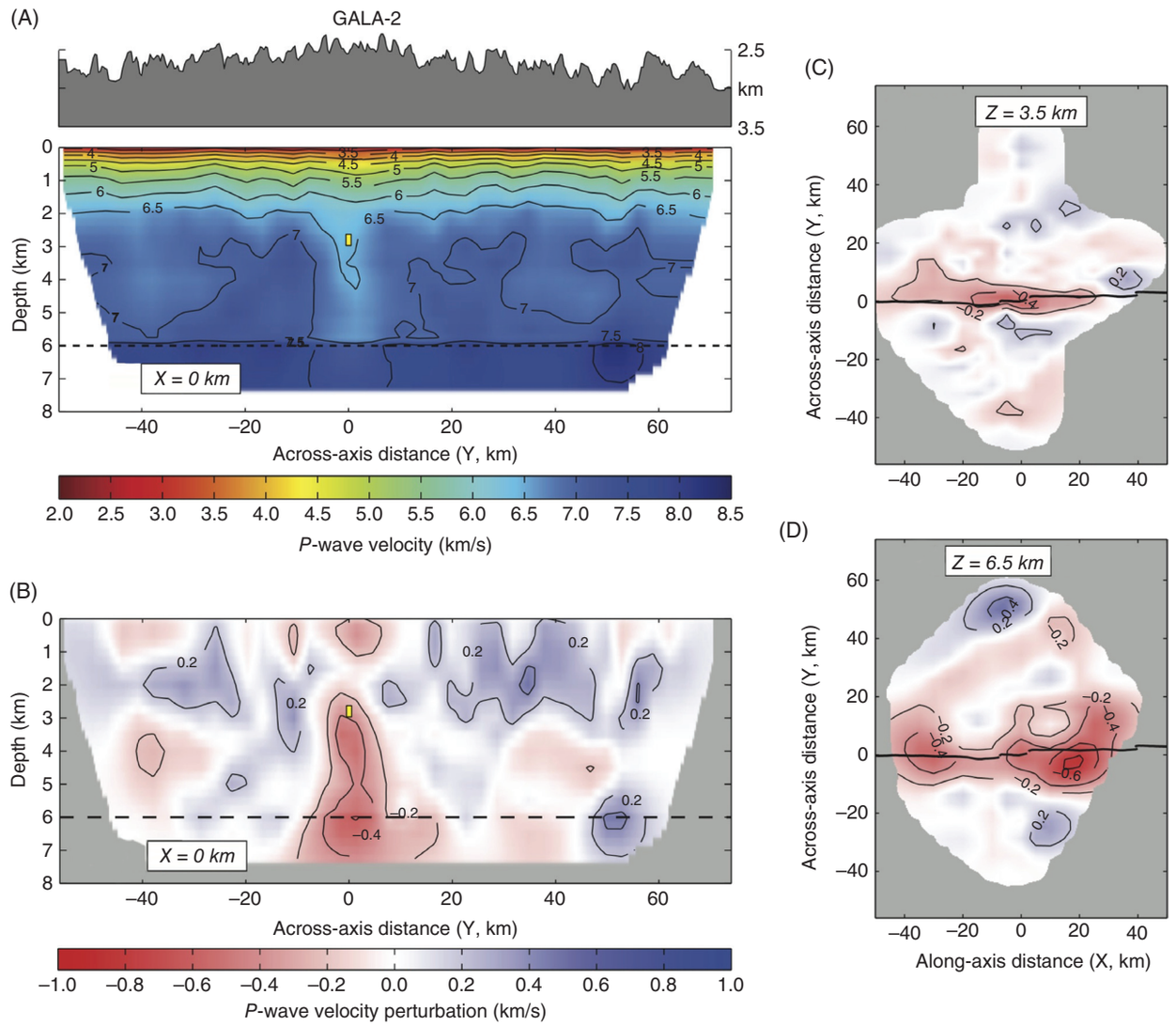

Figure 17.10 Preferred 3D model for GALA-2. (A) *P*-wave velocity model along the main NS profile ($X = 0$ km), with contours every 0.5 km/s. Dashed line corresponds to the Moho reflector. Panel on top shows the bathymetry along the profile. (B) *P*-wave velocity variations with respect to the starting 1D model contoured every 0.2 km/s. Yellow rectangle in A and B shows the depth and width of the AML reflector imaged by *Blacic et al.* [2004]. C and D show depth slices of the velocity perturbation at 3.5 and 6.5 km depth, respectively. Solid line shows the spreading axis.

17.5.3. GALA-3

Upper crustal structure (0–1 km depth) across the GALA-3 area shows lower velocities within 10 km of the axis, compared to older crust (Figure 17.11A, B). At greater depths beneath the ridge axis we image an axial LVZ 6–7 km in width. This LVZ shows distinct local maxima at different levels throughout the crust. The highest-amplitude anomaly (5.1 km/s at 1.5 km depth at the axis, compared to 6.0 km/s at similar depth off-axis; Figure 17.11A) is located 1.5–2.0 km bsf and coincides with the location of the imaged AML reflector (Figure 17.11B). Deeper in the crust, between 3 and 4 km bsf, we find another velocity anomaly with 6.5 km/s, compared to 7.0 km/s in older crust at similar depths (Figure 17.11B). This lower crustal velocity anomaly is centered beneath the ridge axis in the sections where we have data coverage (Figure 17.11C). Based on synthetic resolution tests (Appendix), the observation of a localized lower crustal anomaly does not seem to be a model artifact, due to uneven ray sampling with depth; a test of a uniformly spread axial velocity anomaly does not produce such localization of anomalies (Figure 17.A3).

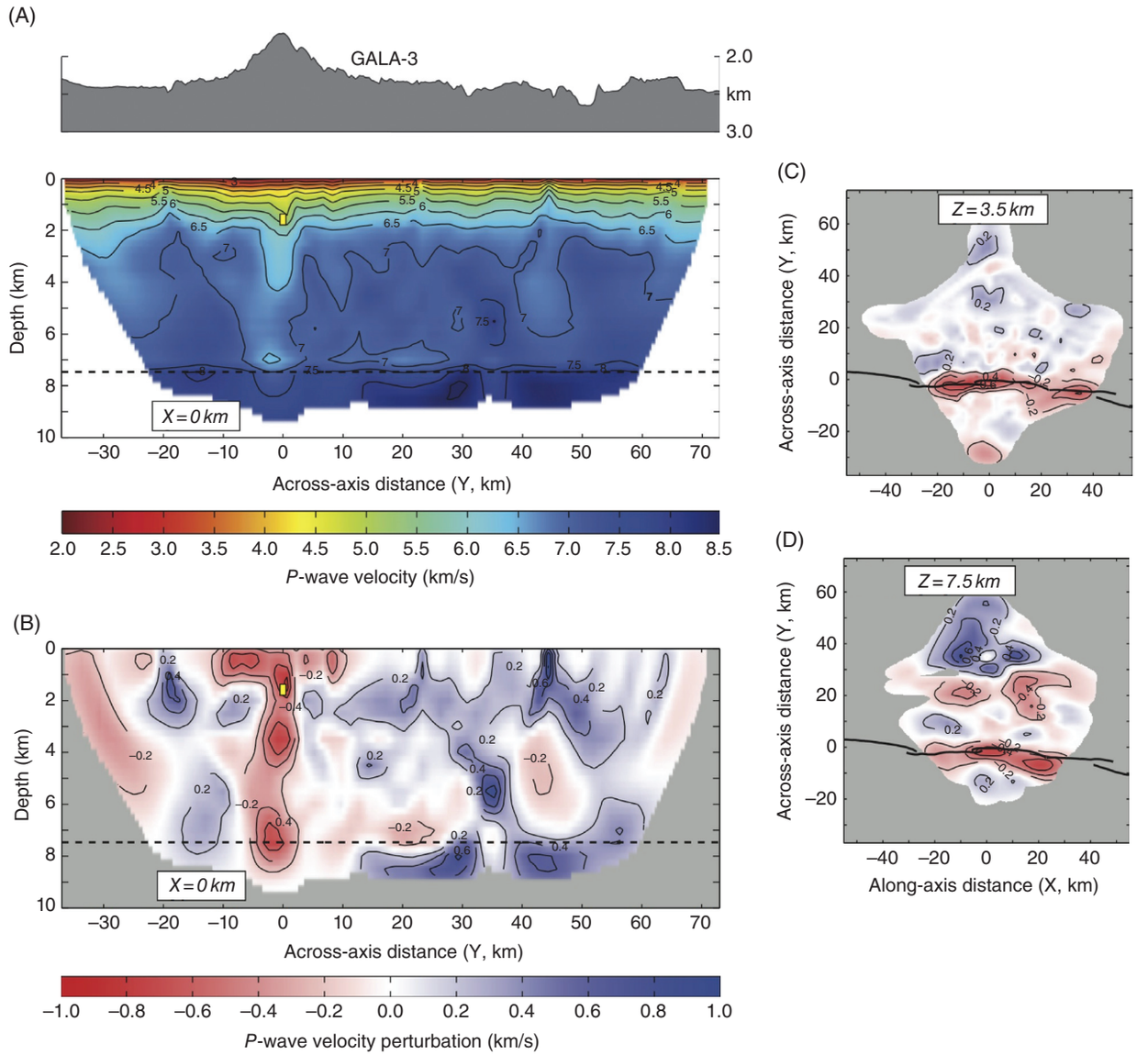

Figure 17.11 Preferred 3D model for GALA-3. (A) *P*-wave velocity model along the main NS profile ($X = 0$ km), with contours every 0.5 km/s. Dashed line corresponds to the Moho reflector. Panel on top shows the bathymetry along the profile. (B) *P*-wave velocity variations with respect to the starting 1D model contoured every 0.2 km/s. Yellow rectangle in A and B shows the depth and width of the AML reflector imaged by *Blacic et al.* [2004]. (C) and (D) show depth slices of the velocity perturbation at 3.5 and 7.5 km depth, respectively. Solid line shows the spreading axis.

At the Moho, the axial LVZ presents a local anomaly with maximum amplitude between 7 and 8 km depth. This anomaly extends along the ridge axis, but it is slightly shifted to the south of the axis (Figure 17.11D). The axial LVZ does not appear to extend down deeper into the mantle, but this could be due to lack of sufficient ray coverage at those depths (8–9 km bsf).

17.6. INTERPRETATION

The focus of this study is to quantify the distribution of melt in the crust beneath a mid-ocean ridge as a function of magma supply. For this reason, we restrict the interpretation of our preferred models to the axial LVZ. Other features observed in the models are easily

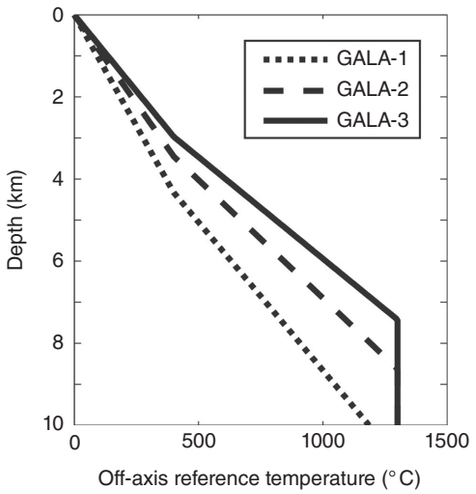

Figure 17.12 Reference thermal structures for off-axis crust at the three sites. These thermal structures were obtained from an *ad hoc* thermal model that takes into account the shape of the axial LVZ and axial lithospheric thickness [*Ito and Behn*, 2008].

explained by other processes, such as crustal aging. For example, the increase in upper crustal velocity with increasing distance from the ridge axis observed across GALA-2 and GALA-3 is consistent with reduction in shallow porosity due to aging and precipitation of hydrothermally derived minerals [e.g., *Grevemeyer and Weigel*, 1997]. Additionally, our models contain both shallow and deeper local crustal anomalies away from the ridge axis (e.g., Figure 17.11B). Some of them are spatially related to off-axis faults (Figures 17.9 and 11), while others could be artifacts of the model produced by the tomography method due to the fact that our experimental geometry was not designed for 3D imaging. We do not attempt to interpret those features.

17.6.1. Thermal structure

Within the axial zone, *P*-wave velocities lower than those of mature crust are primarily caused by elevated temperatures and possibly partial melt within the accretionary zone. To estimate the distribution of melt in the crust, we follow the general approach of *Dunn et al.* [2000] by first constructing a thermal model and removing thermal effects from the seismic models. The model geothermal profiles include a low geothermal gradient in the shallowest crust (from 0–400 °C) to simulate efficient cooling by hydrothermal circulation [*Phipps Morgan and Chen*, 1993] and a steeper gradient—appropriate for conductive cooling—between 400 °C and 1,300 °C, following the simple *ad hoc* approach of *Ito and Behn* [2008]. The model geothermal profiles (Figure 17.12) are designed to correspond to a reference 1D thermal structure approximately 20 km off-axis. The model geothermal profiles are derived by assuming that the 1,300 °C isotherm is at the depths of the AML reflectors beneath GALA-2 and GALA-3. At GALA-1, we choose the Moho (5.5 km) as the depth to the axial 1,300 °C isotherm, given the presence of a deep axial valley and observed global trends of AML depth with axial morphology [*Ito and Behn*, 2008]. The 1,300 °C isotherm is assumed to deepen (with 400 °C being 40% as deep) away from the ridge axis, having depths shown in Figure 17.12.

Variations in temperature about the reference geotherms with cross-axis distance and depth are then computed from the seismic tomography models following *Dunn et al.* [2000]. The partial derivative of temperature with respect to V_P is the sum of a frequency-independent anharmonic component representing thermal expansion and a frequency-dependent anelastic component that takes into account crystal relaxation and friction [e.g., *Karato*, 1993; *Karato and Karki*, 2001]. The parameters used for this calculation (Equation 3 in *Dunn et al.* [2000]) are indicated in Table 17.3. The attenuation structure is defined as $Q = 1000$ everywhere in the model except for $Q = 40$ [*Wilcock et al.*, 1995] in a trapezoidal axial zone whose width increases with depth from 1 km at the depth of the AML reflector to 8.7 km, 11.3 km, and 13.3 km for GALA-1, 2, and 3, respectively, at 10 km depth. The geometry of this low-Q region mimics the 1,300 °C isotherm of the thermal model within the axial zone.

17.6.2. Estimated melt content

After converting the axial velocity anomalies to thermal anomalies as described above, we considered that partial melt could only be present in regions where temperatures exceed those of the liquidus temperature calculated as T_L [°C] = 19.1XMgO [wt%] + 1,054 [*Sinton and Detrick*, 1992]. We adopted an MgO value of 8 wt% as representative for the three study areas [*Cushman et al.*, 2004]. The effect on velocity of temperatures below T_L was removed from the observed velocity anomalies, and the residual velocity anomalies were then attributed to the effects of melt.

We estimate the melt content from the residual velocity anomalies (i.e., after removing temperature effects) for two possible cases of melt distribution within the rock matrix: tubules and thin melt films. Microtomography of partially molten peridotite reveals that melt is distributed in interconnected melt channels along grain edges [*Zhu et al.*, 2011] whose topology can be approximated as tubules [*Smith*, 1964]. We use the formulation developed by *Mavko* [1980] to relate this melt topology to changes in elastic parameters of partially molten rocks. Using the elastic parameter values listed in Table 17.4, we obtain a V_P dependence on melt fraction ϕ for crustal and mantle rocks for melt distributed in tubules (Table 17.3).

Table 17.3 Elastic, thermal, and melt content relations and constants.

Relation	Value	Definition	Reference
$\left[\frac{\partial \ln V_P}{\partial T}\right]_{\text{crust, anharmonic}}$	$-8.1 \cdot 10^{-5}\,\text{K}^{-1}$	Partial derivative of V_P with respect to temperature	[*Christensen*, 1979]
$\left[\frac{\partial \ln V_P}{\partial T}\right]_{\text{mantle, anharmonic}}$	$-6.2 \cdot 10^{-5}\,\text{K}^{-1}$		[*Isaak*, 1992]
F	1	See *Karato* [1993]	[*Karato*, 1993]
H^*_{crust}	$276\,\text{kJ mol}^{-1}$	Activation enthalpy	[*Caristan*, 1982]
H^*_{mantle}	$500\,\text{kJ mol}^{-1}$		[*Jackson et al.*, 1992]
$\left[\frac{\partial \ln V_P}{\partial \phi}\right]_{\text{gabbro, melt in tubules}}$	−0.74	Partial derivative of V_P with respect to melt fraction	[*Mavko*, 1980]
$\left[\frac{\partial \ln V_P}{\partial \phi}\right]_{\text{peridotite, melt in tubules}}$	−0.86		[*Mavko*, 1980]
$\left[\frac{\partial \ln V_P}{\partial \phi}\right]_{\text{melt in films}}$	−3		[*Dunn et al.*, 2000; *Schmeling*, 1985]

Table 17.4 Elastic parameters used for calculating $\frac{\partial \ln V_P}{\partial \phi}$ for melt in tubules.

Variable	Value	Definition	Reference
$[K]_{\text{gabbro}}$	$0.859 \cdot 10^{11}$ Pa	Bulk modulus	[*Miller and Christensen*, 1997]
$[K]_{\text{peridotite}}$	$1.16 \cdot 10^{11}$ Pa		[*Christensen*, 1966]
$[\mu]_{\text{gabbro}}$	$0.43 \cdot 10^{11}$ Pa	Shear modulus	[*Miller and Christensen*, 1997]
$[\mu]_{\text{peridotite}}$	$0.57 \cdot 10^{11}$ Pa		[*Christensen*, 1966]
$[\eta]_{\text{gabbro}}$	0.286	Poisson ratio	[*Miller and Christensen*, 1997]
$[\eta]_{\text{peridotite}}$	0.29		[*Christensen*, 1966]
$[\rho]_{\text{gabbro}}$	$2{,}912\,\text{kg m}^{-3}$	Density	[*Miller and Christensen*, 1997]
$[\rho]_{\text{peridotite}}$	$3{,}290\,\text{kg m}^{-}3$		[*Christens*en, 1966]
$[\rho]_{\text{melt}}$	$2{,}700\,\text{kg m}^{-3}$		[Hooft and *Detrick*, 1993]
$[V_P]_{\text{melt}}$	$3{,}300\,\text{m s}^{-1}$	*P*-wave velocity	[*Singh et al.*, 1998]

A recent study of melt distribution in partially molten peridotite using high-resolution imaging concluded that melt along grain boundaries (i.e., thin films) is the dominant geometry, with tubule geometries being present but small compared to the film geometries [*Garapić et al.*, 2013]. For this case, we adopt the V_P dependence on melt fraction ϕ for relaxed films reported by *Dunn et al.* [2000], based on the formulation of *Schmeling* [1985] (Table 17.3).

Estimates of the melt fraction within the axial zone for the three study areas are shown in Figure 17.13, for both of the melt geometries considered. At the GALA-1 site, our estimates show a mid-crustal zone at 2–3 km depth with melt fractions of up to 8% if the melt is contained in tubules (2% for melt in films; hereinafter we report melt fractions for the tubules case, followed by the corresponding melt fraction for films in parentheses). This result

occurs in spite of our assumption of 1,300 °C being well below the Moho in our reference geotherm model (a hotter geotherm would yield estimates of even more melt), and suggests either an inconsistency between the adopted reference thermal model and the seismic tomography model or, most likely, that the mid-crustal velocity anomaly beneath GALA-1 is not related to elevated temperatures and presence of melt. This will be discussed in more detail in "Confidence of melt in the crust and alternative explanations" (below). At GALA-1, no melt is required deeper in the crust between this anomaly and the Moho, even if in this region velocities are approximately 0.4 km/s slower than off-axis values (Figure 17.9B). Immediately below the Moho we find a broad zone (approximately 12 km wide) containing just a few percent of melt, with a maximum of 6% (2%) located 2–4 km to the north of the ridge axis.

At the GALA-2 area our velocity models do not predict much detectable melt within the axial crust, perhaps just 1–2% (less than 1%) between 4 and 6 km depth. Most or all of crustal velocity anomaly shown in Figure 17.10B can be explained by temperature alone. Most notable is the lack of a body of partial melt (of sufficient volume or concentration to be detected) at the level of the imaged AML reflector (Figure 17.13). Below the Moho, however, we find a broad zone of just a few percent melt extending as far as 10 km off-axis, encompassing an approximately 6-km-wide zone where the melt content is highest at 6% (2%), centered at the ridge axis.

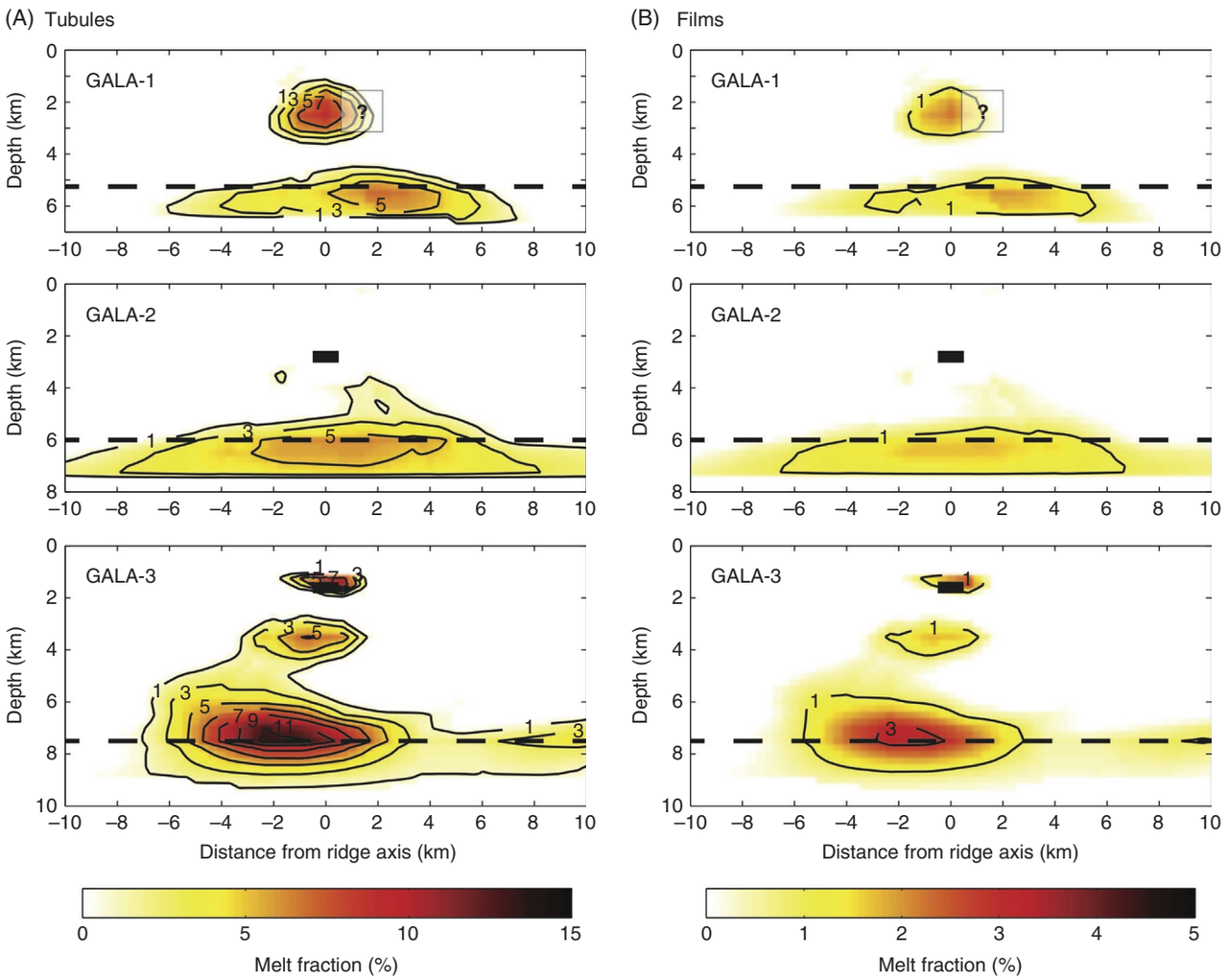

Figure 17.13 Estimates of melt fraction in the axial zone derived from the tomography results for both of the melt geometries considered: (A) melt in tubules; (B) melt in thin films. Contours of melt fraction are numbered every 2%. Dashed line corresponds to the Moho. The black rectangles in GALA-2 and –3 show the depth of the AML reflector.

At the GALA-3 area we find three distinct zones of melt accumulation: at 1.0–1.5 km depth, a lower-crustal zone at 3–4 km depth, and a deeper zone extending from 5–9 km depth at the base of the crust and uppermost mantle (Figure 17.13). These melt zones are not vertically aligned with each other, but rather show a progressive shift toward the south flank of the ridge axis with depth. The shallowest zone is narrow (1–2 km), it is coincident with the seismically imaged AML reflector, and it contains up to 10% (3%) melt. The lower-crustal melt zone is slightly wider (3–4 km) and centered 1 km off-axis, with up to 7% (2%) melt content. The deeper and larger melt zone (extending up to 10 km to the north of the axis) contains up to 13% (3%) melt, and its maximum content occurs in a 8-km-wide zone centered 2 km to the south of the axis. A connection between the lower-crustal melt zone and the shallower one is not evident (i.e., no melt is detected between the two zones), but a few percent melt within the lower crust is seen to link this lower-crustal melt body with the deeper reservoir at the Moho (Figure 17.13).

17.6.3. Confidence of melt in the crust and alternative explanations

A source of uncertainty in our estimates of melt is the assumed off-axis reference geothermal profile (Figure 17.12). For example, at GALA-3 the sub-AML LVZ could be fully explained by thermal effects alone if we assume that the temperature at the Moho 20 km off-axis is less than 400 °C, which is unrealistically low for such young crust. At shallower levels, even the extreme case of assuming an off-axis thermal model with constant $T = 0$ °C at all depths would result in predictions of melt present at the AML level beneath GALA-3. Therefore, we can conclude that the crustal/mantle levels where our seismic models predict melt are well constrained, although the magnitude of the melt estimates within these regions may change by a few percent if alternative, realistic off-axis thermal models are adopted. For example, the off-axis (0.7 Myr) temperature at the Moho for GALA-3 predicted by a plate cooling model [*Stein and Stein*, 1992] is 1,134 °C. Using this alternative thermal reference model, we obtain melt content estimates for GALA-3 (Figure 17.A5) that are just less than 2% lower than those of the preferred model (Figure 17.13). On the other hand, tomography methods tend to underestimate the amplitude of velocity anomalies (Appendix). This effect probably results in our preferred melt contents to be underestimated by approximately 2% (Figure 17.A5). Thus, the effects of using an upper bound reference thermal structure (i.e., warm, off-axis crust) and underestimating axial velocity anomalies are of the same order of magnitude but opposite sign, and therefore cancel each other.

The assumed thermal structure at the ridge axis used to derive the off-axis reference geotherm has little impact on melt estimates. For example, if the temperature at the AML is 1,350 °C instead of 1,300 °C, as we have assumed, melt fraction estimates would be less than 0.6% higher than our preferred estimates (Figure 17.13).

Our resolution tests (Appendix, Figures 17.A1–A4) indicate that the differences in axial seismic structure (and therefore in estimated melt crustal distribution) between the three study areas are not an artifact resulting from the different experimental geometries and data quality between the three study areas. At GALA-1 and GALA-2, where our models do not predict melt within the lower crust, melt still could be present at such depths in small pockets of high melt fraction, but its average concentration within the lower crustal volume should be less than approximately 1% to be consistent with our observations. Therefore, we conclude that the lack of detectable melt content in the lower crust at GALA-1 and GALA-2 does not reflect limitations of the experimental design and tomography modeling at these sites compared to GALA-3.

At the GALA-1 site, we have interpreted the low velocity anomaly at 2–3 km depth as resulting from elevated temperature and melt. However, this interpretation is at odds with observations at the Juan de Fuca Ridge, Eastern Lau Spreading Center, and the middle section of the WGSC—all where magma is imaged by AML reflectors at comparable depths—but where the ridge axis has transitional morphology or small topographic highs, not a deep axial valley like at GALA-1 [*Ito and Behn* 2008]. One possible explanation is that the observations at GALA-1 represent an atypical situation of seismology detecting a recent, short-lived magma intrusion that will eventually cool and solidify rapidly compared to the longer time scale over which axial morphology develops, as it has been inferred at other slow-spreading segments [e.g., *Canales et al.*, 2000a].

Alternatively, the shallow LVZ at GALA-1 may represent a zone of increased porosity and fracturing within the axial valley, a common observation at a slow-spreading segment with rift valley morphology [e.g., *Dunn et al.*, 2005]. In addition, our resolution tests (Appendix) indicate that our ability to detect low-velocity zones in the mid-crust at GALA-1 is limited, and that the imaging method may introduce artifacts such as leakage of deeper velocity anomalies into the upper crust. For these reasons, our interpretation of this crustal velocity anomaly as representing up to 8% melt (Figure 17.13) should be taken as an end-member case, with other explanations being plausible.

17.7. DISCUSSION AND CONCLUSIONS

The difference in spreading rate between the study areas is negligible, but their magma supply is significantly different (Table 17.5). This difference in magma supply arises from variation in mantle melt productivity along the GSC produced by its proximity to the Galápagos hotspot [*Canales et al.*, 2002]. The differences in axial crustal structure that we observe between the three sites are a direct consequence of the larger extent of plume influence along the ridge from west to east. Therefore, magma supply, rather than spreading rate, is a better parameter to represent the variety of crustal structures which we observe at the WGSC, and can be used to compare our results to those from other mid-ocean ridges.

17.7.1. Melt below the Moho

Our results indicate that at the three study areas, the largest melt reservoir is located at or just below the Moho (Figures 17.13 and14), consistent with previous geophysical and geochemical results [*Crawford and Webb*, 2002; *Dunn et al.*, 2000; *Wanless and Shaw*, 2012]. Melt fraction and volume of melt per km of ridge within this sub-crustal reservoir increases from GALA-1 to GALA-3 as magma supply increases (Figures 17.13 and 17.14, Table 17.5). Accumulation of melt at the Moho is probably controlled by the formation of permeability barriers. These barriers may form as porous flow from the mantle [*Aharonov et al.*, 1995; *Kelemen et al.*, 1995] enters a conductively cooling regime, favoring the formation of anorthosite bands, plagioclase-clinopyroxene-orthopyroxene saturation within crystallizing gabbros, or formation of low porosity cumulate gabbros after melt extraction [*Kelemen and Aharonov*, 1998; *Korenaga and Kelemen*, 1998].

17.7.2. Melt distribution in the lower crust as a function of magma supply

Models for GALA-1 and GALA-2 do not require the presence of melt within the lower crust (Figure 17.13). This contrasts with results from GALA-3, where we

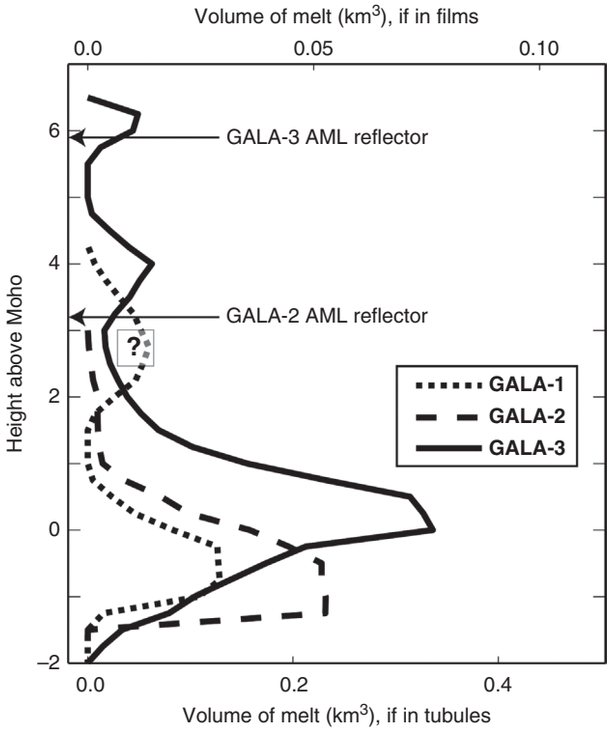

Figure 17.14 Estimates of volume of melt per km of ridge as a function of height above the Moho.

Table 17.5 Crustal structure parameters at several spreading centers.

Location	*SR*	Z_{crust}	Z_{AML}	*M*	ϕ_{lc}	V_{Moho}	References
MAR, Lucky Strike	22	7.5	3.0	1.7	[c]	[c]	[e]
MAR, OH-1 35°N	22	8.5	[a]	1.9	3	[d]	[f]
GSC, GALA-1	53	5.25	[b]	2.8	[c]	0.03–0.13	This study
GSC, GALA-2	56	6.0	2.8	3.3	[c]	0.05–0.23	This study
MAR, South Iceland	20	20	[a]	4.0	[c]	[c]	[g]
GSC, GALA-3	57	7.5	1.6	4.3	2–13	0.08–0.34	This study
EPR, 9°30′N	114	7.5	1.6	8.5	3–16	0.08–0.29	[h]

SR: Full spreading rate (mm yr^{-1}).; Z_{crust}: Crustal thickness (km); Z_{AML}: Depth to AML reflector (km); *M*: Magma supply per km of ridge (10^5 m^3 yr^{-1} km^{-1}), defined as $M = Z_{crust} \times SR$ [e.g., *Sinton et al.*, 2003]; ϕ_{lc}: Melt content in the lower crust (%).; V_{Moho}: Volume of melt per km of ridge at the Moho (km^3).

[a] Surveyed but not found.
[b] Not surveyed.
[c] Not required.
[d] Not reported.
[e] [*Seher et al.*, 2010; *Singh et al.*, 2006]
[f] [*Canales et al.*, 2000b; *Dunn et al.*, 2005; *Hooft et al.*, 2000; *Hussenoeder et al.*, 2002]
[g] [*Bjarnason et al.*, 1993]
[h] [*Dunn et al.*, 2000; *Kent et al.*, 1993]

estimate that between the shallow melt lens and the Moho there is a few percent melt distributed throughout the crust with a lower crustal reservoir at 3–4 km depth containing up to 7% melt (Figure 17.3).

With the main melt reservoir located at the Moho, a lower magma supply (Table 17.5) at GALA-1 and GALA-2 may result in less frequent upward migration of melt from the Moho reservoir to crustal levels, leading to a lower crustal section that is largely solidified and cooler than at GALA-3, where melt supply is higher. This is supported by the finding of less pronounced axial velocity anomalies below the AML at GALA-2 than at GALA-3. In this sense, the AML at GALA-2 could be a thin and isolated melt body that is undetectable by our tomography experiment, yet with enough melt in it to produce the necessary impedance contrast to be detected by MCS imaging [*Blacic et al.*, 2004]. At this location, transport of melt from the base of the crust to the shallow AML is probably dominated by diking events that can transport melt above the Moho to a freezing horizon where the shallow melt lens forms [*Hooft and Detrick*, 1993; *Phipps Morgan and Chen*, 1993].

At a regime with greater magma supply like GALA-3, the transfer of melt from the mantle to the crust may occur more frequently (as porous flow [*Aharonov et al.*, 1995; *Kelemen et al.*, 1995] and/or diking [*Boudier et al.*, 1996; *Kelemen et al.*, 1997]), favoring the formation of intermediate-depth melt reservoirs like the one we detect at 4 km above the Moho at GALA-3. This intermediate-depth reservoir would ultimately feed the shallower melt lens.

Our interpretation is consistent with global trends in MOR basalt compositions, which suggest that ridges with high melt supply produce magmas that have much greater variation in chemical signatures imparted by differentiation in the crust [*Rubin and Sinton*, 2007]. On the other end of the spectrum, lower melt supply produces magma of more uniform differentiation because they reside in fewer thermally isolated reservoirs deeper in the crust [*Rubin and Sinton*, 2007]. Our results indicate that at these low melt-supply settings, the main magma reservoir is located at the Moho, while other crustal reservoirs are probably episodic and short-lived.

17.7.3. Comparisons with other spreading segments

Comparison of our results with those from similar studies at other spreading centers allows us to place our interpretations within the broader context of magma supply. Table 17.5 summarizes our findings and those from the Lucky Strike segment at the MAR [*Seher et al.*, 2010], MAR segment OH-1 [*Dunn et al.*, 2005], a subaerial portion of the MAR in southern Iceland [*Bjarnason et al.*, 1993], and EPR 9°30′N [*Dunn et al.*, 2000]. Although this dataset is limited, we find that the larger volumes of melt at the Moho reservoir occur beneath ridges where magma supply is approximately above 4×10^5 $m^3\ yr^{-1}$ per km of ridge axis (GALA-3 and EPR 9°30′N; Table 17.5). In addition, these high-magma supply examples are, with the exception of segment OH-1, the only ones where available seismic data predict the presence of melt in the lower crust. In this regard, of particular interest are the results from southern Iceland, where the seismic models do not require the presence of crustal magma chamber(s) thicker than 500 m [*Bjarnason et al.*, 1993], despite a magma supply slightly lower than at GALA-3 due to the combination of considerably thick crust (20 km) and slow spreading rate (Table 17.5). Therefore, based on this limited dataset, it seems that there is a transition at a magma supply of approximately $4.0–4.3\times10^5$ $m^3\ yr^{-1}\,km^{-1}$, above which a large melt reservoir at the Moho can sustain sufficiently frequent transfer of melt to the crust and development of multiple crustal reservoirs, and below which transfer of melt through the lower crust is infrequent so little melt is present over geologically appreciable timescales. More studies of crustal melt distribution at different magma supplies will be needed to confirm this inference.

It is unclear why MAR segment OH-1, with a magma supply of $1.9\times10^5\ m^3\ yr^{-1}\,km^{-1}$, is an outlier from the simple relationship between magma supply and crustal melt distribution which we have inferred. *Dunn et al.* [2005] suggest that the lower crustal velocity and anisotropy anomaly at OH-1 are best explained by the presence of molten dikes intruding a hot, but melt-free, lower crust. This interpretation is consistent with the model described above, and thus it is possible that the crustal structure at OH-1 represents an episodic magmatic event and is therefore a temporal anomaly. Alternatively, interpretation of OH-1 results could be biased, due to a lack of a realistic thermal reference model valid for that location. In our study and others, uncertainty in near-axis thermal structure is one of the main factors affecting crustal melt content estimates from seismic velocities. Overestimation of off-axis crustal temperatures may lead to misinterpreting velocity anomalies of thermal origin as requiring the presence of melt. A better understanding of near-axis thermal structure will be needed in the future to improve constraints on crustal melt distribution beneath mid-ocean ridges.

17.8. APPENDIX: RESOLUTION TESTS

17.8.1. Checkerboard tests

We conduct checkerboard tests to gain insight about the resolution of our models in the axial zone. On the background 1D velocity models (Figure 17.5) we imposed alternate positive and negative velocity anomalies (±0.6 km/s) 3-km-thick and 10-km-wide within 20 km of

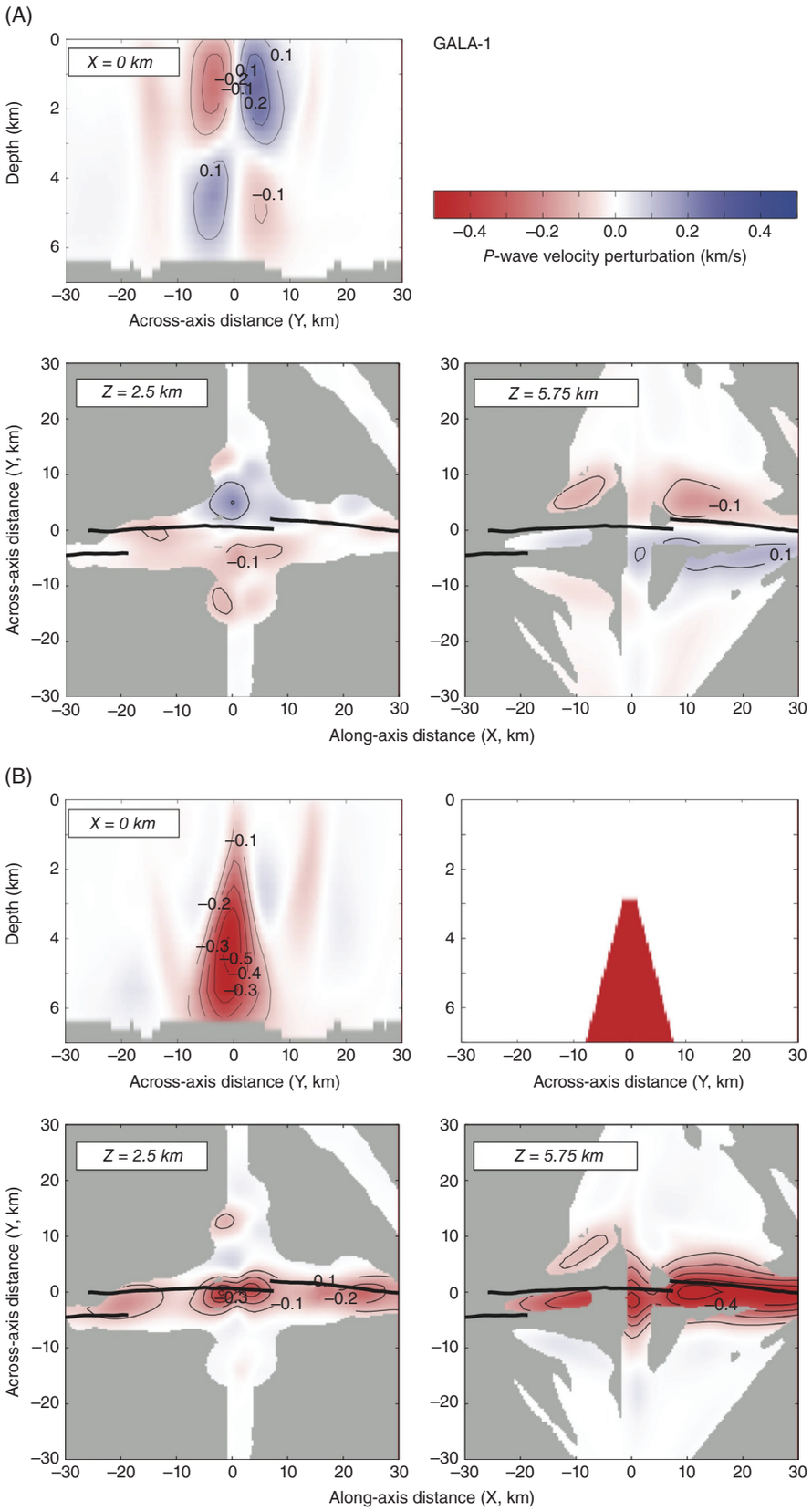

Figure 17.A1 (A) Results of a checkerboard test for site GALA-1. The synthetic velocity perturbation is formed by 10-km-wide, 3-km-thick alternating positive and negative velocity anomalies (anomalies have constant value in the ridge-parallel direction for a given depth). Anomalies are only imposed within 10 km of the ridge axis. (B) Synthetic case testing the resolvability of a ridge-centered triangular low-velocity anomaly. Top right shows the true anomaly, and the other panels show the recovered anomaly.

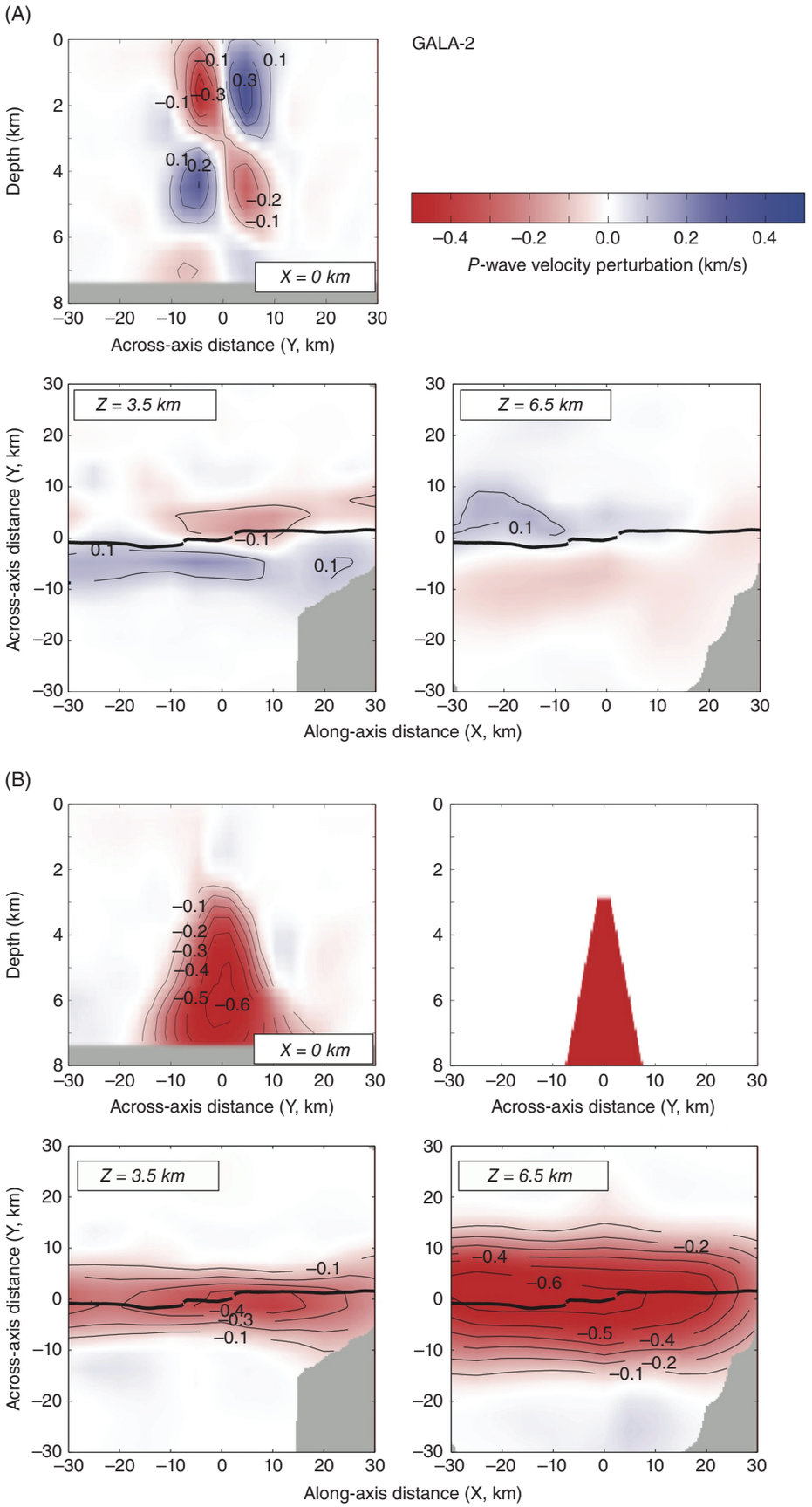

Figure 17.A2 Same as A1 for GALA-2.

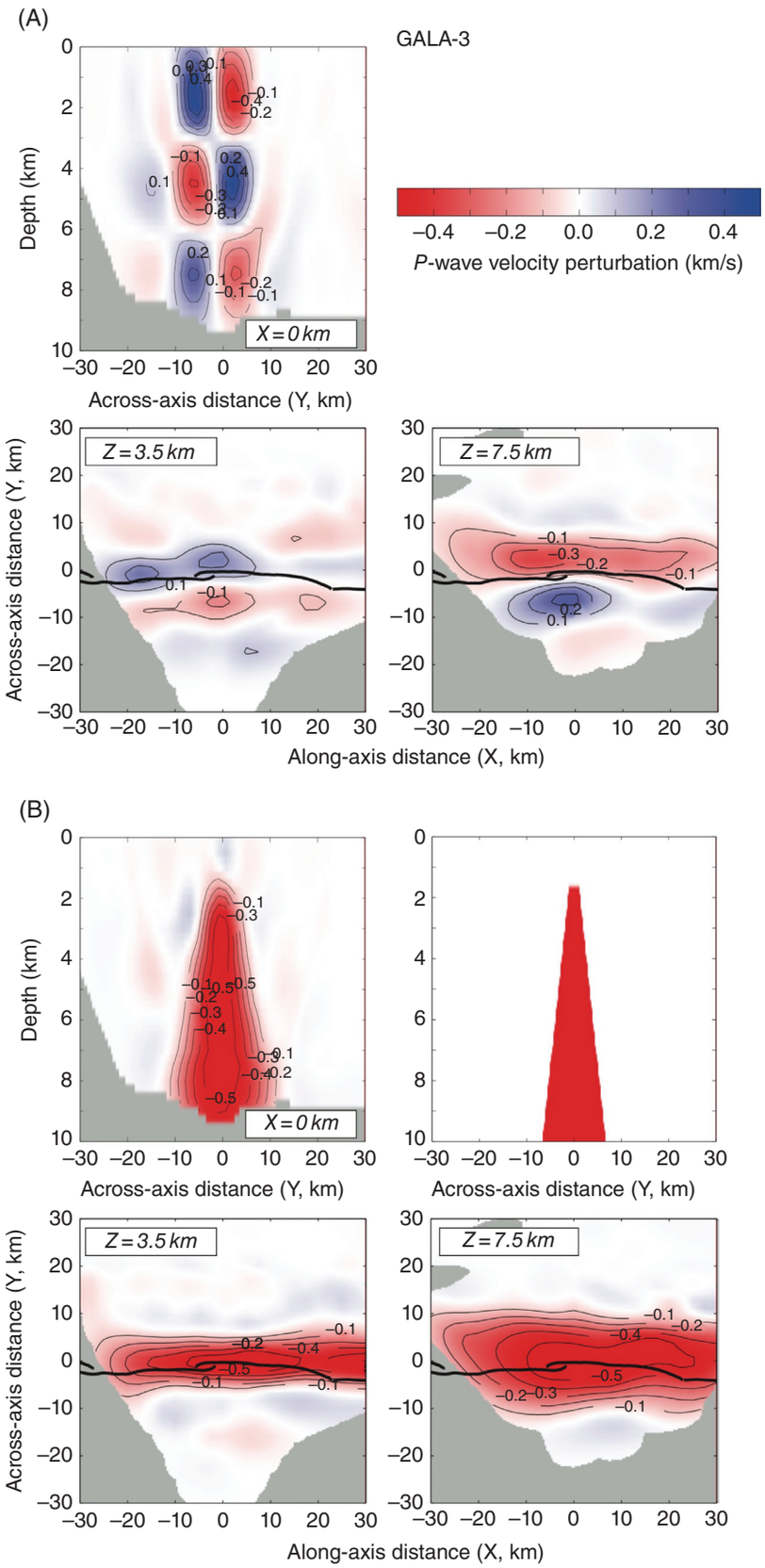

Figure 17.A3 Same as A1 for GALA-3.

the ridge axis. The anomalies are constant in the along-axis direction (i.e., they resemble horizontal cylinders parallel to the ridge axis). We then inverted the synthetic travel times with the same assigned uncertainty as the observed data (but with no added noise) using our experimental geometry and the same inversion parameters as our preferred models (except that only one iteration was conducted). At GALA-1, this test shows that resolution at this scale is good in the upper 3 km of the crust (Figure 17.A1A). At lower crustal and Moho levels, the test shows that the size of the anomalies is reasonably well-recovered, but the recovered amplitude is greatly diminished with respect to the true anomaly. At GALA-2 (Figure 17.A2A), resolution across the axis is quite good at all crustal levels, although the amplitude of the imaged anomalies in the lower crust is less than 50% than the true anomaly. At GALA-3 (Figure 17.A3A) resolution is very good at all crustal levels beneath the ridge axis. These tests also show that along-axis resolution at the three sites is restricted to the location of the main NS profiles ($X = 0$ km, Figure 17.A1A).

17.8.2. Axial low-velocity anomaly tests

In order to gain insight into how much of the differences we find on axial crustal structure between the three study areas could be due to differences in acquisition geometry and data quality, we conducted a test in which we imposed a triangular low-velocity zone at the ridge axis on a background 1D velocity model (Figure 17.5). The synthetic models all have similar anomalies (−0.6 km/s) that are 1 km wide at the depth of the AML reflector (for GALA-1 we used 2.8 km, same as for GALA-2) and increase in width with depth so that they are 10 km wide at Moho depths (Figures 17.A1B, A2B, and A3B). The tests show that at all three sites we can resolve reasonably well the shape of the axial low velocity zone, although the magnitude of the recovered anomalies vary between sites (Figure 17.A4), and in some cases show smearing outside of the boundaries of the anomalies (e.g., GALA-1, Figure 17.A1B).

Figure 17.A4 shows the true and recovered velocity anomalies at the ridge axis ($X = 0$ km, $Y = 0$ km) for the three sites. At GALA-3 and GALA-2 we find that our dataset is able fully recover the anomaly throughout most of the crust, from the mantle to approximately 1 km below the AML. At GALA-1 our test can only partially recover the amplitude of the anomaly within the lower 2 km of the crust, and at shallower levels the recovered anomaly is smeared up and leaks into the upper crust. These tests suggest that our tomographic results probably underestimate the magnitude of the axial velocity anomalies, and therefore our crustal melt content estimates probably represent lower bounds. For example, the

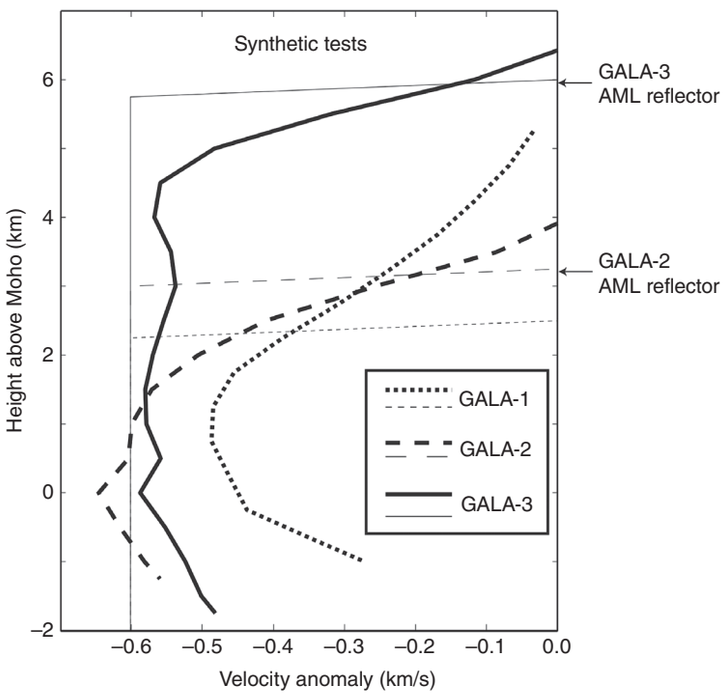

Figure 17.A4 One-dimensional velocity anomaly profiles extracted from the models shown in Figures 17.A1B, A2B, and A3B at $X = 0$ km and $Y = 0$ km. Both true (thin lines) and recovered anomalies (thick lines) are shown. Velocity anomalies are shown relative to height above the Moho depth.

GALA-3 test shows that 90% of the amplitude of the velocity anomaly is recovered within most of the axial crust (Figure 17.A4), while at GALA-2 and GALA-1 only approximately 80% and approximately 70%, respectively, of the axial velocity anomalies within the 2 km of crust above the Moho are recovered (Figure 17.A.4). To quantify the possible bias in melt content estimates introduced by a likely underestimate of the magnitude of velocity anomalies, we recalculated melt fractions assuming that the velocity anomalies shown in Figures 17.9–11 represent 70%, 80%, and 90% of the true velocity anomalies at GALA-1, -2, and −3, respectively. These new melt

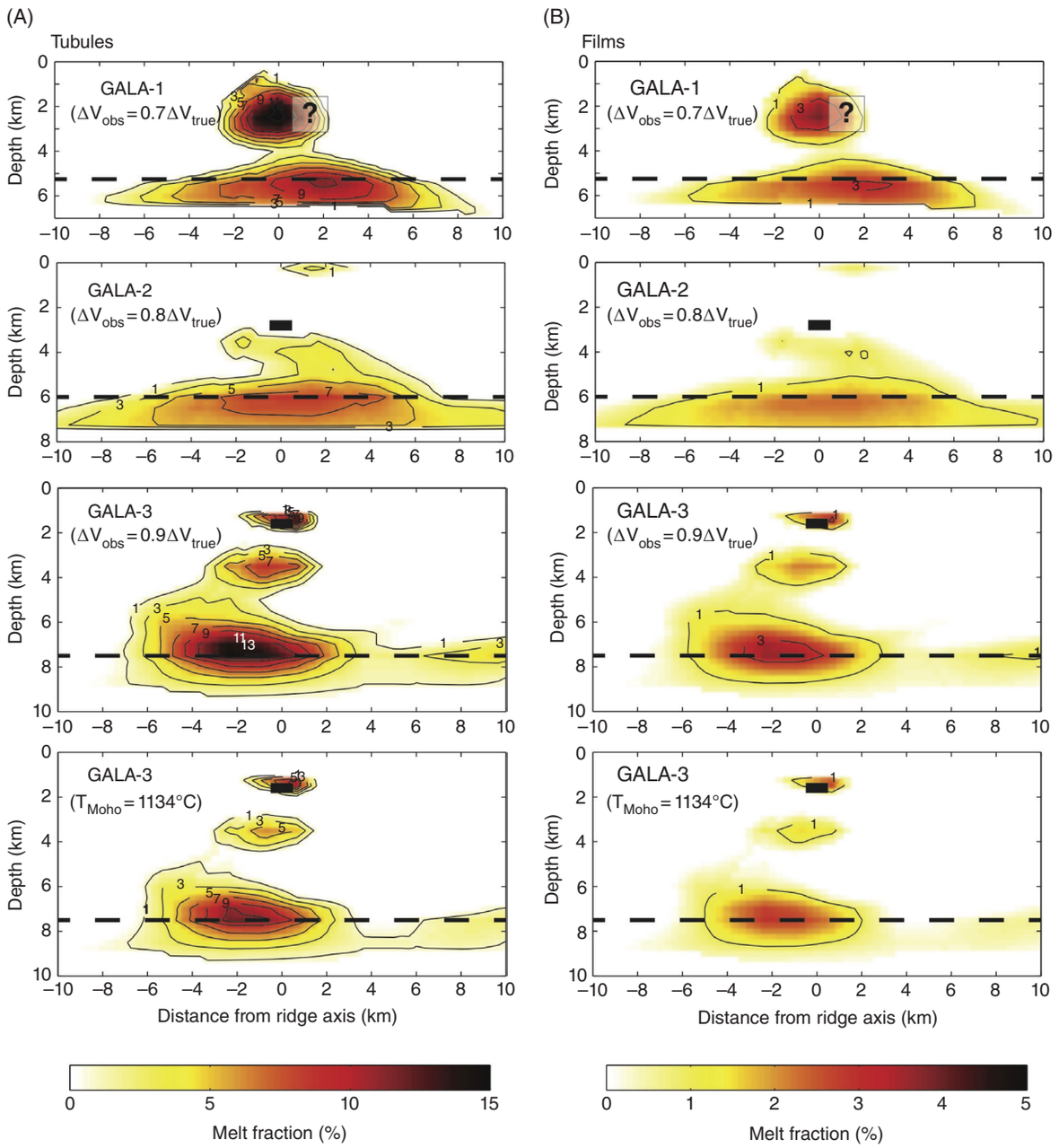

Figure 17.A5 Estimates of melt fraction as in Figure 17.13, except that the velocity anomalies used for the thermal and melt calculations are assumed to be 70%, 80%, and 90% of the "true" velocity anomalies for GALA-1, -2, and –3, respectively. Also shown at the bottom are estimates for GALA-3, assuming that the off-axis temperature at the Moho is 1,134 °C, as predicted by a plate cooling model for 0.7 Ma crust [*Stein and Stein*, 1992], instead of 1,300 °C as in the preferred model (Figure 17.12).

fraction estimates are shown in Figure 17.A5. While the distribution of crustal melt does not differ from our preferred models, the melt content estimates are approximately 2% larger if the velocity anomalies were underestimated by the amounts indicated above.

17.9. ACKNOWLEDGMENTS

This research was supported by NSF grants OCE-9819117 and OCE-0327289 to the Woods Hole Oceanographic Institution, and OCE-0327051 to University of Hawai′i. We thank Ecuadorian authorities for granting us permission to work within Ecuador's exclusive economic zone, and the WHOI OBS Group for their technical support and efforts during data acquisition.

REFERENCES

Aharonov, E., J. Whitehead, P.B. Kelemen, and M. Spiegelman (1995), Channeling instability of upwelling melt in the mantle, *J. Geophys. Res.*, *100*, 20, 433–20, 450.

Baker, E.T. et al. (2008), High-resolution surveys along the hot-spot-affected Galápagos Spreading Center: 1. Distribution of hydrothermal activity, *Geochem. Geophys. Geosyst.*, *9*, Q09003, doi:10.1029/2008GC002028.

Baran, J.M., J.R. Cochran, S.M. Carbotte, and M.R. Nedimović (2005), Variations in upper crustal structure due to variable mantle temperature along the Southeast Indian Ridge, *Geochem. Geophys. Geosyst.*, *6*(11), Q11002, doi:10.1029/2005GC000943.

Behn, M.D., J.M. Sinton, and R.S. Detrick (2004), Effect of the Galápagos hotspot on seafloor volcanism along the Galápagos Spreading Center (90.9–97.6°W), *Earth Planet. Sci. Lett.*, *217*, 331–347.

Bjarnason, I.T., W. Menke, O.G. Flóvenz, and D. Caress (1993), Tomographic image of the Mid-Atlantic plate boundary in southwestern Iceland, *J. Geophys. Res.*, *98* (B4), 6607–6622.

Blacic, T.M., G. Ito, J.P. Canales, R.S. Detrick, and J.M. Sinton (2004), Constructing the crust along the Galápagos Spreading Center 91.3–95.5°W: Correlation of seismic layer 2A with axial magma lens and topographic characteristics, *J. Geophys. Res.*, *109*, B10310, doi:10.1029/2004JB003066.

Blacic, T.M., G. Ito, A.K. Shah, J.P. Canales, and J. Lin (2008), Axial high topography and partial melt in the crust and mantle beneath the western Galápagos Spreading Center, *Geochem. Geophys. Geosyst.*, *9*, Q12005, doi:10.1029/2008GC002100.

Boudier, F., A. Nicolas, and B. Ildefonse (1996), Magma chambers in the Oman ophiolite: fed from the top and the bottom, *Earth Planet. Sci. Lett.*, *144*, 239–250.

Bown, J.W., and R.S. White (1994), Variation with spreading rate of oceanic crustal thickness and geochemistry, *Earth Planet. Sci. Lett.*, *121*, 435–449.

Braun, M.G., and R.A. Sohn (2003), Melt migration in plume-ridge systems, *Earth Planet. Sci. Lett.*, *213*, 417–430.

Canales, J.P. et al. (1997), Variations in axial morphology along the Galápagos spreading center and the influence of the Galápagos hotspot, *J. Geophys. Res.*, *102*, 27,341–27,354.

Canales, J.P., J.A. Collins, J. Escartín, and R.S. Detrick (2000a), Seismic structure across the rift valley of the Mid-Atlantic Ridge at 23°20′N (MARK area): Implications for crustal accretion processes at slow spreading ridges, *J. Geophys. Res.*, *105*, 28,411-28,425.

Canales, J.P., R.S. Detrick, J. Lin, J.A. Collins, and D.R. Toomey (2000b), Crustal and upper mantle seismic structure beneath the rift mountains and across a non-transform offset at the Mid-Atlantic Ridge (35°N), *J. Geophys. Res.*, *105*, 2699–2719.

Canales, J.P., G. Ito, R.S. Detrick, and J.M. Sinton (2002), Crustal thickness along the western Galápagos Spreading Center and the compensation of the Galápagos hotspot swell, *Earth Planet. Sci. Lett.*, *203* (1), 311–327.

Caristan, Y. (1982), The transition from high temperature creep to fracture in Maryland diabase, *J. Geophys. Res.*, *87* (B8), 6781–6790.

Christensen, N.I. (1966), Elasticity of ultrabasic rocks, *J. Geophys. Res.*, *71*, 5921–5931.

Christensen, N.I. (1979), Compressional wave velocities in rocks at high temperatures and pressures, critical thermal gradients, and crustal low-velocity zones, *J. Geophys. Res.*, *84*, 6849–6857.

Christensen, N.I., and M.H. Salisbury (1979), Seismic anisotropy in the oceanic upper mantle: evidence from the Bay of Islands ophiolite complex, *J. Geophys. Res.*, *84* (B9), 4601–4610.

Christie, D.M., R. Werner, F. Hauff, K. Hoernle, and B.B. Hanan (2005), Morphological and geochemical variations along the eastern Galápagos Spreading Center, *Geochem. Geophys. Geosyst.*, *6* (1), Q01006.

Crawford, W.C., and S.C. Webb (2002), Variations in the distribution of magma in the lower crust and at the Moho beneath the East Pacific Rise at 9–10°N, *Earth Planet. Sci. Lett.*, *203* (1), 117–130.

Cushman, B., J.M. Sinton, G. Ito, and J.E. Dixon (2004), Glass compositions, plume-ridge interaction, and hydrous melting along the Galápagos Spreading Center, 90.5°W to 98°W, *Geochem. Geophys. Geosyst.*, *5* (8), Q08E17, doi:10.1029/2004GC000709.

Detrick, R.S. et al. (2002), Correlated geophysical, geochemical and volcanological manifestations of plume-ridge interaction along the Galápagos Spreading Center, *Geochem. Geophys. Geosyst.*, *3* (10), 8501, doi:10.1029/2002GC000350.

Dunn, R.A., and D.R. Toomey (2001), Crack-induced seismic anisotropy in the oceanic crust across the East Pacific Rise (9°30′N), *Earth Planet. Sci. Lett.*, *189*, 9–17.

Dunn, R.A., and D.W. Forsyth (2007), Crust and Lithospheric Structure—Seismic Structure of Mid-Ocean Ridges, in *Treatise in Geophysics*, edited by B. Romanowicz and A.M. Dziewonski, pp. 419–443.

Dunn, R.A., D.R. Toomey, and S.C. Solomon (2000), Three-dimensional seismic structure and physical properties of the crust and shallow mantle beneath the East Pacific Rise at 9°30′N, *J. Geophys. Res.*, *105*, 23,537-23,555.

Dunn, R.A., V. Lekic, R.S. Detrick, and D.R. Toomey (2005), Three-dimensional seismic structure of the Mid-Atlantic Ridge (35°N): Evidence for focused melt supply and lower crustal dike injection, *J. Geophys. Res.*, *110*, B09101.

Garapić, G., U.H. Faul, and E. Brisson (2013), High-resolution imaging of the melt distribution in partially molten upper mantle rocks: evidence for wetted two-grain boundaries, *Geochem. Geophys. Geosyst.*, *14* (3), 556–566.

Grevemeyer, I., and W. Weigel (1997), Increase of seismic velocities in upper oceanic crust: The "superfast" spreading East Pacific Rise at 14°14′S, *Geophys. Res. Lett.*, *24* (3), 217–220.

Harpp, K.S., and D.J. Geist (2002), Wolf-Darwin lineament and plume-ridge interaction in northern Galápagos, *Geochem. Geophys. Geosyst.*, *3* (11), 8504, doi:10.1029/2002GC000370.

Haymon, R.M. et al. (2008), High-resolution surveys along the hot spot–affected Gálapagos Spreading Center: 3. Black smoker discoveries and the implications for geological controls on hydrothermal activity, *Geochem. Geophys. Geosyst.*, *9*, Q12006, doi:10.1029/2008GC002114.

Hey, R.N. (1977), Tectonic evolution of the Cocos-Nazca spreading center, *Geol. Soc. Am. Bull.*, *88*, 1404–1420.

Hey, R.N., and P.R. Vogt (1977), Spreading center jumps and sub-axial asthenosphere flow near the Galápagos hotspot, *Tectonophys.*, *37*, 41–52.

Hey, R.N., G.L. Johnson, and A. Lowrie (1977), Recent plate motions in the Galápagos area, *Geol. Soc. Am. Bull.*, *88*, 1385–1403.

Hey, R.N., F.K. Dunnebier, and W.J. Morgan (1980), Propagating rifts on mid-ocean ridges, *J. Geophys. Res.*, *85*, 3647–3658.

Hey, R.N., M.C. Kleinrock, S.P. Miller, T.M. Atwater, and R.C. Searle (1986), Sea Beam/deep-tow investigation of an active oceanic propagating rift system Galápagos 95.5 W, *J. Geophys. Res.*, *91*, 3369–3393.

Hooft, E.E.E., and R.S. Detrick (1993), The role of density in the accumulation of basaltic melts at mid-ocean ridges, *Geophys. Res. Lett.*, *20* (6), 423–426.

Hooft, E.E.E., R.S. Detrick, D.R. Toomey, J.A. Collins, and J. Lin (2000), Crustal and upper mantle structure along three contrasting spreading segments of the Mid-Atlantic Ridge, 33.5–35°N, *J. Geophys. Res.*, *105*, 8205–8226.

Hussenoeder, S.A., G.M. Kent, and R.S. Detrick (2002), Upper crustal seismic structure of the slow spreading Mid-Atlantic Ridge, 35°N: Constraints on volcanic emplacement processes, *J. Geophys. Res.*, *107* (B8), 2156.

Ingle, S. et al. (2010), Mechanisms of geochemical and geophysical variations along the western Galápagos Spreading Center, *Geochem. Geophys. Geosyst.*, *11*, Q04003, doi:10.1029/2009GC002694

Isaak, D.G. (1992), High-temperature elasticity of iron-bearing olivines, *J. Geophys. Res.*, *97* (B2), 1871–1885.

Ito, G., and J. Lin (1995), Mantle temperature anomalies along the present and paleoaxes of the Galápagos Spreading Center as inferred from gravity analyses, *J. Geophys. Res.*, *100*, 3733–3745.

Ito, G., and M.D. Behn (2008), Magmatic and tectonic extension at mid-ocean ridges: 2. Origin of axial morphology, *Geochem. Geophys. Geosyst.*, *9*, Q09O12, doi:10.1029/2008GC001970.

Ito, G., J. Lin, and D.W. Graham (2003), Observational and theoretical studies of the dynamics of mantle plume-mid-ocean ridge interaction, *Rev. Geophys.*, *41* (4), doi:10. 1029/2002RG000117.

Jackson, I., M.S. Paterson, and J.D. Fitz Gerald (1992), Seismic wave dispersion and attenuation in Aheim dunite: an experimental study, *Geophys J. Int.*, *108*, 517–534.

Karato, S. (1993), Importance of anaelasticity in the interpretation of seismic tomography, *Geophys. Res. Lett.*, *20*, 1623–1626.

Karato, S., and B.B. Karki (2001), Origin of lateral variation of seismic wave velocities and density in the deep mantle, *J. Geophys. Res.*, *106* (B10), 21771–21783.

Kelemen, P.B., and E. Aharonov (1998), Periodic formation of magma fractures and generation of layered gabbros in the lower crust beneath oceanic spreading ridges, in *Faulting and Magmatism at Mid-Ocean Ridges*, edited by W.R. Buck, P.T. Delaney, J.A. Karson and Y. Lagabrielle, pp. 267–289, AGU, Washington, D.C.

Kelemen, P.B., N. Shimizu, and V.J.M. Salters (1995), Extraction of mid-ocean ridge basalt from the upwelling mantle by focused flow of melt in dunite channels, *Nature*, *375*, 747–753.

Kelemen, P.B., K. Koga, and N. Shimizu (1997), Geochemistry of gabbro sills in the crust-mantle transition zone of the Oman ophiolite: Implications for the origin of the oceanic lower crust, *Earth Planet. Sci. Lett.*, *146*, 475–488.

Kent, G.M., A.J. Harding, and J.A. Orcutt (1993), Distribution of magma beneath the East Pacific Rise between the Clipperton transform and the 9°17′N deval from forward modeling of common depth point data, *J. Geophys. Res.*, *98*, 13,945-13,969.

Kokfelt, T.F., C. Lundstrom, K. Hoernle, F. Hauff, and R. Werner (2005), Plume–ridge interaction studied at the Galápagos spreading center: Evidence from ^{226}Ra–^{230}Th–^{238}U and ^{231}Pa–^{235}U isotopic disequilibria, *Earth Planet. Sci. Lett.*, *234*, 165–187.

Korenaga, J., and P.B. Kelemen (1998), Melt migration through the oceanic lower crust: a constraint from melt percolation modeling with finite solid diffusion, *Earth Planet. Sci. Lett.*, *156*, 1–11.

Mavko, G.M. (1980), Velocity and attenuation in partially molten rocks, *J. Geophys. Res.*, *85* (B10), 5173–5189.

Miller, D.J., and N.I. Christensen (1997), Seismic velocities of lower crustal and upper mantle rocks from the slow spreading Mid-Atlantic Ridge, south of the Kane transform zone (MARK), in *Proc. ODP, Sci. Results*, edited by J.A. Karson, M. Cannat, D.J. Miller and D. Elthon, pp. 437–454, College Station, TX (Ocean Drilling Program).

Mittelstaedt, E., and G. Ito (2005), Plume-ridge interaction, lithospheric stresses, and the origin of near-ridge volcanic lineaments, *Geochem. Geophys. Geosyst.*, *6* (6), Q06002, doi:10.1029/2004GC000860.

Morgan, W.J. (1978), Rodriguez, Darwin, Amsterdam,.., a second type of hotspot island, *J. Geophys. Res.*, *83*(B11), 5355–5360.

Parson, L.M. et al. (1993), En echelon axial volcanic ridges at the Reykjanes Ridge: a life cycle of volcanism and tectonics, *Earth Planet. Sci. Lett.*, *117*, 73–87.

Phipps Morgan, J., and Y.J. Chen (1993), The genesis of oceanic crust: Magma injection, hydrothermal circulation, and crustal flow, *J. Geophys. Res.*, *98*, 6283–6297.

Purdy, G.M., L.S.L. Kong, G.L. Christeson, and S.C. Solomon (1992), Relationship between spreading rate and the seismic structure of mid-ocean ridges, *Nature*, *355*, 815–817.

Rotella, M.D., J.M. Sinton, J. Mahoney, and W. Chazey (2009), Geochemical evidence for low magma supply and inactive propagation at the Galápagos 93.25°W overlapping spreading center, *Geochem. Geophys. Geosyst.*, *10*, Q09005, doi:10.1029/2009GC002445.

Rubin, K.H., and J.M. Sinton (2007), Inferences on mid-ocean ridge thermal and magmatic structure from MORB compositions, *Earth Planet. Sci. Lett.*, *260*, 257–276.

Schilling, J.-G., R.H. Kingsley, and J.D. Devine (1982), Galápagos hot spot-spreading center system 1. Spatial petrological and geochemical variations (83°W–101°W), *J. Geophys. Res.*, *87* (B7), 5593–5610.

Schilling, J.-G., D. Fontignie, J. Blichert-Toft, R.H. Kingsley, and U. Tomza (2003), Pb-Hf-Nd-Sr isotope variations along the Galápagos Spreading Center (101–83°W): Constraints on the dispersal of the Galápagos mantle plume, *Geochem. Geophys. Geosyst.*, *4* (10), 8512, doi:10.1029/2002GC000495.

Schmeling, H. (1985), Numerical models on the influence of partial melt on elastic, anelastic and electric properties of rocks. Part I: elasticity and anelasticity, *Phys. Earth Planet. In.*, *41*, 34–57.

Seher, T. et al. (2010), Crustal velocity structure of the Lucky Strike segment of the Mid-Atlantic Ridge at 37°N from seismic refraction measurements, *J. Geophys. Res.*, *115*, Q03011.

Shearer, P.M. (1999), *Introduction to Seismology*, Cambridge University Press, Cambridge.

Singh, S.C., G.M. Kent, J.S. Collier, A.J. Harding, and J.A. Orcutt (1998), Melt to mush variations in crustal magma properties along the ridge crest at the southern East Pacific Rise, *Nature*, *394*, 874–878.

Singh, S.C. et al. (2006), Discovery of a magma chamber and faults beneath a Mid-Atlantic Ridge hydrothermal field, *Nature*, *442*, 1029–1032.

Sinton, J.M., and R.S. Detrick (1992), Mid-ocean ridge magma chambers, *J. Geophys. Res.*, *97*, 197–216.

Sinton, J.M., R.S. Detrick, J.P. Canales, G. Ito, and M. Behn (2003), Morphology and Segmentation of the Western Galápagos Spreading Center, 90.5°98°W: Plume-Ridge Interaction at an Intermediate Spreading Ridge, *Geochem. Geophys. Geosyst.*, *4* (12), 8515, doi:10.1029/2003GC000609.

Smith, C.S. (1964), Some elementary principles of polycrystalline microstructure, *Met. Rev.*, *9*, 1–48.

Smith, W.H.F., and D.T. Sandwell (1997), Global seafloor topography from satellite altimetry and ship depth soundings, *Science*, *277*, 1957–1962.

Sohn, R.A., S.C. Webb, J.A. Hildebrand, and B.D. Cornuelle (1997), Three-dimensional tomographic velocity structure of upper crust, CoAxial segment, Juan de Fuca Ridge: Implications for on-axis evolution and hydrothermal circulation, *J. Geophys. Res.*, *102* (B8), 17,679-17,695.

Stein, C.A., and S. Stein (1992), A model for the global variation in oceanic depth and heat flow with lithospheric age, *Nature*, *359*, 123–129.

Toomey, D.R., D. Jousselin, R.A. Dunn, W.S.D. Wilcock, and R.S. Detrick (2007), Skew of mantle upwelling beneath the East Pacific Rise governs segmentation, *Nature*, *446*, 409–414.

Wanless, V.D., and A.M. Shaw (2012), Lower crustal crystallization and melt evolution at mid-ocean ridges, *Nat. Geosci.*, *5*, 651–655.

White, S.M. et al. (2008), High-resolution surveys along the hot spot–affected Galápagos Spreading Center: 2. Influence of magma supply on volcanic morphology, *Geochem. Geophys. Geosyst.*(*9*), Q09004, doi:10.1029/2008GC002036.

Wilcock, W.S.D., S.C. Solomon, G.M. Purdy, and D.R. Toomey (1995), Seismic attenuation structure of the East Pacific Rise near 9°30'N, *J. Geophys. Res.*, *100*, 24,147-24,165.

Wilson, D.S., and R.N. Hey (1995), History of rift propagation and magnetization intensity for the Cocos-Nazca spreading center, *J. Geophys. Res.*, *100* (B6), 10,041-10,056.

Zhu, W., G.A. Gaetani, F. Fusseis, L.G.J. Móntesi, and F. De Carlo (2011), Microtomography of partially molten rocks: three-dimensional melt distribution in mantle peridotite, *Science*, *332*, 88–91.